Part One Basic Methodology

Infrared and Raman Spectroscopic Imaging. Edited by Reiner Salzer and Heinz W. Siesler

ISBN: 978-3-527-31993-0

1
Infrared and Raman Instrumentation for Mapping and Imaging

Peter R. Griffiths

1.1
Introduction to Mapping and Imaging

The analysis of localized regions of samples by vibrational microspectroscopy can be accomplished in two ways, by mapping or imaging.

Mapping involves the sequential measurement of the spectra of adjacent regions of a sample. This is achieved by moving each region of that sample into the beam focus of a microscope after the spectrum of the previous region has been measured; the measurement is then repeated until the entire region of interest has been covered.

Imaging, on the other hand, requires an image of the sample to be focused onto an array detector, where the intensity of the radiation passing through each region of the sample is measured at each pixel. In a mapping experiment in which the sample is only moved in one direction – say the x direction – the measurement is called line mapping. If the sample is moved in both the x and y dimensions, the measurement cannot be properly called imaging, as the spectra have not been acquired by an array detector. However, the spectra that are obtained can be treated in exactly the same way as if they had been acquired with an array detector.

In hyperspectral imaging, the images at more than ten wavelength regions are recorded simultaneously with a two-dimensional (2-D) array detector. Vibrational hyperspectral imaging can be accomplished through the measurement of either the mid-infrared, near-infrared (NIR) or Raman spectrum. The measurement of each type of spectrum is accomplished in different ways, although the instruments that have been developed for the measurement of NIR and Raman spectra are more closely related than are mid-infrared hyperspectral imaging spectrometers. In NIR and Raman instruments, the signal at a given wavelength is recorded at each pixel. In NIR imaging instruments, the light is usually passed through a monochromator or narrow band-pass filter (e.g., a liquid crystal tunable filter) before being focused on the sample, and from there onto the array detector. The image from one wavelength region is measured at all pixels simultaneously. The wavelength region is then changed (usually, but not necessarily, to an adjacent

Infrared and Raman Spectroscopic Imaging. Edited by Reiner Salzer and Heinz W. Siesler

ISBN: 978-3-527-31993-0

spectral region) and the intensity at each pixel is measured again. This process is repeated until all wavelengths of interest in the spectrum have been measured.

An analogous approach is used for Raman imaging, except that the monochromator must be located after the sample. The signal from all pixels for a given wavelength setting is acquired rapidly in NIR imaging instruments, where the signal-to-noise ratio (SNR) is usually high. The SNR for Raman imaging is much lower, so that a much longer integration time is needed. Thus, Raman imaging can be painfully slow unless only a few wavelength regions are measured. In both NIR and Raman imaging spectrometers, the bandpass of the monochromator or filter determines the spectral resolution. Occasionally, only a short spectral range or a few wavelength regions may be sufficient to classify samples that are composed of just a few components. On the other hand, for complex or previously uncharacterized samples, it is usually necessary to measure data over the entire spectral range. In mid-IR imaging instruments, it is more common to couple the array to an interferometer, so that interferograms from different spatial regions of the sample are recorded at each detector element. Subsequent Fourier transformation yields the desired hyperspectral data set. All types of systems will be described in this chapter.

In addition to the mapping and imaging approaches outlined above, a hybrid technique is also available where a linear array of detectors is used to measure the spectra over a line of points on a sample simultaneously, so that a line image is measured. By using the same approach as for mapping measurements, and with a single-element detector, the sample is moved after each measurement so that the spectra of the next linear region of interest are measured. The spectra are then 'stitched' together to form the complete image. This 'push-broom' approach has proved to be useful for mid-IR imaging (as will be discussed later in the chapter). Of course, it may well be that even the region that can be monitored with a 2-D array detector (especially the smaller arrays, such as 16×16 pixels) does not cover the entire sample of interest. In that case, the sample is also moved after each measurement so that a hyperspectral image of the adjacent region is acquired. These data can then also be stitched together (a procedure sometimes known as *quilting* or *mosaicing*) to allow an image to be observed over a wider area.

The end result of either spectroscopic mapping or hyperspectral imaging is an array of spectra (sometimes called a hyperspectral cube) from which the identifying characteristics of inhomogeneous samples can be obtained. For Raman imaging, the sample need not be of constant thickness, although ideally it should be as flat as possible. Conversely, when mid-IR or NIR absorption spectra are to be measured, the thickness of the sample should be as uniform as possible. In this case, it is sometimes possible to synthesize an image that shows the concentration of a certain component by simply plotting the absorbance at a certain wavelength of a band that is isolated from all others in the spectrum (e.g., the C≡N stretching mode of polyacrylonitrile, *vide infra*; Figure 1.24). If this approach proves to be feasible, the image may either be plotted as a gray scale, with white representing the absence of the component and dark gray representing its greatest concentration, or – more commonly nowadays – through the use of color.

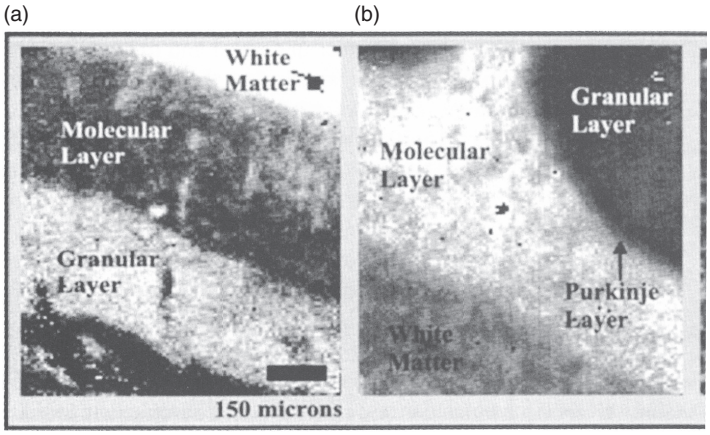

Figure 1.1 Infrared spectroscopic gray-scale images of thin cerebellar sections from (a) a control rat and (b) a rat treated with the drug cytarabine, showing the spatial distribution of lipid and protein by ratioing the absorbance of the CH_2 antisymmetric stretching band at 2927 cm^{-1} and the N–H stretching band at 3350 cm^{-1}. Reproduced with permission from Ref. [1].

It is usually not possible to obtain samples of absolutely constant thickness, and in this case the ratio of the peak absorbance or integrated absorbance of bands that can be assigned to particular components must be calculated [1, 2]. An example of this approach can be seen in Figure 1.1, which shows the infrared images of thin cerebellar sections from an untreated rat and a rat treated with the drug cytarabine. The images demonstrate the spatial distribution of lipid and protein by ratioing the absorbance of the CH_2 antisymmetric stretching band at 2927 cm^{-1} and the N–H stretching band at 3350 cm^{-1}. For more complex samples, principal component analysis or more sophisticated chemometric algorithms may be applied (as described in Chapter 2 in this book and also by Diem *et al.* [3] and Šašić and Clark [4]). Although many applications of imaging spectroscopy will be described throughout this volume, only the design of the instruments used to acquire these data will be described in this chapter.

1.2
Mid-Infrared Microspectroscopy and Mapping

1.2.1
Microscopes and Sampling Techniques

Although many noble efforts at fabricating a microscope for infrared spectrometry using a prism monochromator were made during the 1940s and 1950s [5–10], and Perkin-Elmer actually advertised a microscope that could be installed in one of

their prism spectrometers [11], the performance of these instruments was marginal and the use of infrared microscopes never caught on commercially until the early 1990s. Until that time, the mid-IR spectra of minute samples were measured by mounting the sample behind a pinhole of the appropriate dimensions, so that only the region of the sample of interest was irradiated. The sample was then held at the focus of a simple beam condenser that fitted in the sample compartment of the spectrometer. As the size of the region of interest decreased, locating the sample so that the region of interest corresponded to the position of the pinhole became increasingly difficult. However, the situation was dramatically improved when a standard reflecting microscope was interfaced to a Fourier transform infrared (FT-IR) spectrometer. In this case, the previous function of the pinhole was replaced by a remote aperture at a conjugate focus of the sample. A simplified schematic of a typical infrared microscope is shown in Figure 1.2.

The microscope shown in Figure 1.2 is designed to operate in either the transmission or reflection mode. In the transmission mode, the beam from the interferometer is passed onto a toroidal coupling optic and thence to the Cassegrainian condenser. The condenser focuses the beam into a small spot where the sample is mounted. The radiation that is transmitted through the sample is collected by the objective and refocused at a remote adjustable aperture. The part of beam that passes through the aperture is imaged onto an optical viewer (or, more frequently nowadays, a video camera) so that the image of the sample that is passed by the aperture can be viewed. The sample is usually mounted on an *x,y,z* stage The height of the sample is adjusted with the *z* control to ensure that the position of

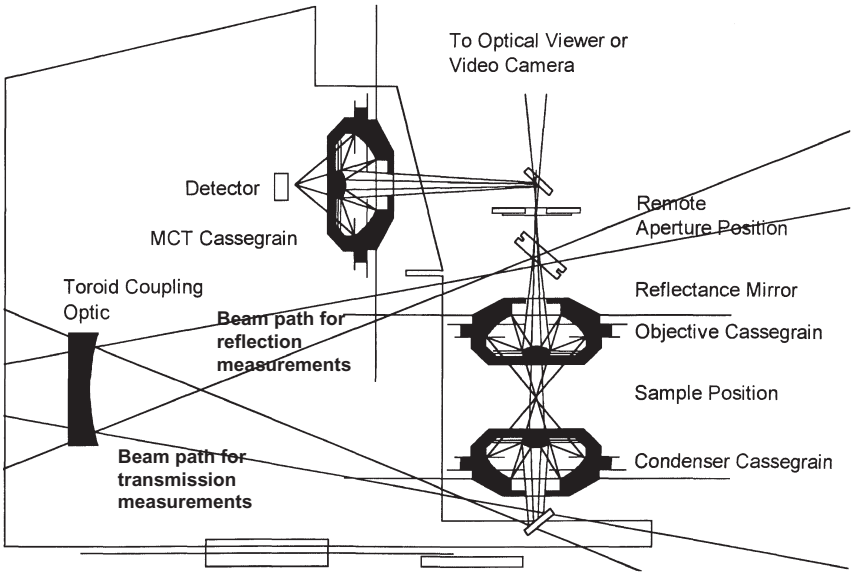

Figure 1.2 Simplified schematic of a typical microscope interfaced to an FT-IR spectrometer. Courtesy of PerkinElmer Inc.

the sample is coincident with the beam focus. The x and y controls are then used to adjust the location of the sample so that the region of interest is at the center of the beam. The jaws of the aperture are then adjusted so that only the region of interest is seen at the viewer. The aperture is often rectangular and can be rotated through 180° to allow the greatest amount of light transmitted through the region of interest in the sample to pass through the aperture. When the conditions have been optimized, a 45° mirror is slid into position so the light that is transmitted through the remote aperture is collected by the third Cassegrain and focused onto the detector, which measures the spectrum of the desired region of the sample.

The condenser goes by two names: some call it a *Cassegrain*, while others call it a *Schwarzschild* objective. The present author has always been rather confused about the difference between a Cassegrain and a Schwarzschild objective but, aiming to resolve such confusion, contacted one of the designers of the first FT-IR microscopes, Bob Messerschmidt (now with Rare Light, Inc.), as to their difference. His reply to this question was as follows:

> The Schwarzschild objective has been used in almost all FT-IR microscopes, and is still used to this day. The design is attributable to the German physicist and astronomer Karl Schwarzschild (1873–1916). The Schwarzschild objective is an all-reflective two-mirror system in which the mirrors are very nearly concentric. The system employs one concave and one convex mirror, and is on-axis, with a hole in one mirror for the light to pass through. The beauty of the system is in its simplicity. It has excellent imaging characteristics over a surprisingly wide field of view, a fact that arises from the mirror concentricity. The first commercial FT-IR microscope, the Digilab IRMA, used this design because the designers were aware that the 1953 Perkin-Elmer microscope for dispersive spectrometers used such a Schwarzschild objective.
>
> The Schwarzschild objective can be considered a special case of a Cassegrainian system. In fact, the Schwarzschild objective is sometimes simply referred to as a Cassegrainian or Cassegrain microscope objective. This name comes from an optical design attributed to Laurent Cassegrain, a Catholic priest who was born in the region of Chartres around 1629 and died in 1693. The invention seems to have occurred in 1672, the same year Isaac Newton reported his first invention, the Newtonian telescope, using a similar yet not the same two-mirror configuration. Most modern telescopes are Cassegrain designs, or very similar. A Cassegrain system is any two-mirror objective with a convex and concave mirror, with a hole in the latter for the light to travel through. There is no requirement of concentricity. So, all Schwarzschild objectives are Cassegrain objectives. The key performance feature of the Schwarzschild design is the concentricity, or near-concentricity, of the two mirrors. It took over 200 years to be invented from the time of Laurent Cassegrain's original design.

When the microscope shown in Figure 1.2 is used in the external reflection mode, the same Cassegrain is used both as the condenser and the objective. In the external reflection mode, the angle at which the toroidal coupling optic is held is switched so that the beam is passed to the top of the objective via a small deflection mirror. The size and location of this mirror are such that half the beam enters the Cassegrain. The beam is demagnified by the primary and secondary mirrors and focused on the sample, which is at the same location as for transmission measurements. The reflected beam is then reconfigured by the secondary and primary mirrors, the optical properties of which are such that the beam misses the small deflection mirror and passes to the remote aperture. Even if a perfect mirror is held at the sample focus, it can be seen that, in comparison to a transmission measurement, only half the signal can be measured when the microscope is used in its reflection mode.

Three types of external reflection spectra can be measured with the microscope optics in the reflection mode shown in Figure 1.2, for which the angle of incidence on the sample is about 30°. In the first type, *transflection spectroscopy* (which is of increasing popularity for mid-IR spectroscopy), a sample of thickness between 5 and 10 μm is deposited on a reflective substrate and the transflection spectrum measured. In measurements of this type, the beam passes through the sample, is reflected from the substrate, and then passes back through the sample before it re-emerges from the surface of the sample and passes to the detector. This type of measurement has occasionally been used for tissue samples, and has proved quite beneficial when the sample is deposited on a 'low-e glass' (low emissivity) slide (Kevley Technologies, Chesterland, OH, USA). These slides, which are fabricated by coating glass with a very thin layer of silver-doped tin oxide, were originally developed for the windows of tall buildings. The coating is thin enough to be transparent to visible light, yet is highly reflective in the mid-IR region. Thus, while any tissue sample on these slides can be inspected by visual microscopy, it still allows the transflection spectrum to be measured [12].

Transflection spectra have the disadvantage that radiation reflected from the front surface of the sample will also reach the detector and give rise to a distortion of the pure transflection spectrum. Merklin and Griffiths [13] showed that the contribution by front-surface reflection can be eliminated by measuring the spectrum at Brewster's angle using p-polarized radiation; that is, radiation polarized such that its electric vector is parallel to the plane of incidence. Brewster's angle for tissue samples is about 50°, which is somewhat higher than the angle of incidence of most infrared microscopes, although the distortion introduced by front-surface reflection will be reduced significantly. It should be noted, however, that the use of a polarizer will reduce the SNR of the spectrum by between a factor of 2 and 3, so this approach may not be beneficial if very small samples, such as single cells, are being investigated.

The other two types of external reflection microspectroscopy are less well suited to the characterization of tissue samples. In the first type, which is variously called *specular reflection*, *front-surface reflection* or *Kramers–Kronig reflection*, the reflectance

spectrum of thick, nonscattering, bulk samples is measured and converted to the wavenumber-dependent optical constants – that is, the refractive index, $n(\tilde{\nu})$ and the absorption index, $k(\tilde{\nu})$ – by the Kramers–Kronig transform, as discussed by Griffiths and de Haseth [14]. As the requirement for the lack of scattering by the sample is essentially never met for tissue samples of the type obtained in medical diagnosis, this will not be discussed further.

The final type of measurement that can be made with the microscope in its reflection mode is diffuse reflection (DR) spectroscopy. Today, very few applications of mid-IR microspectroscopy of neat samples are available, because for mid-IR DR spectrometry the samples should be diluted to a concentration of between 0.5 and 5% with a nonabsorbing diluent (e.g., KBr powder) to preclude band saturation and severe distortion by reflection from the front surface of the particles. However, this mode has substantial application for NIR measurements, where sample dilution is not needed. Because the absorption of NIR radiation by most samples is rather weak, they must either be at least 1 mm thick or be mounted on a reflective or diffusing substrate, such as a ceramic or Teflon disk. In the latter case, the spectrum is caused by a combination of diffuse reflection, transflection and front-surface reflection (hopefully with diffuse reflection being the dominant process).

1.2.2 Detectors for Mid-Infrared Microspectroscopy

Essentially all mid-IR spectra are measured today using FT-IR spectrometers for which the optical path difference (opd) of the interferometers is varied continuously; these are often referred to as 'continuous' or 'rapid-scan' interferometers. Most standard laboratory FT-IR spectrometers are equipped with a 1 mm × 1 mm or 2 mm × 2 mm deuterated triglycine sulfate (DTGS) detector operating at ambient temperature. However, the sensitivity of DTGS detectors is too low to allow them to be used to measure the relatively weak signals encountered after the beam has been passed through the small aperture of a microscope. Instead, the more sensitive liquid-nitrogen-cooled mercury cadmium telluride (MCT) detector is almost invariably used. These detectors operate in the photoconductive mode; that is, when infrared radiation is incident on them the photons promote electrons from the valence band to the conduction band, and the increase in conductivity is a measure of photon flux.

The properties of MCT detectors depend on their composition, that is their Hg:Cd ratio. 'Narrow-band' MCT detectors are typically about 50-fold more sensitive than DTGS, but do not respond to radiation below ~750 cm^{-1}. The cut-off can be extended to a lower wavenumber, but at the expense of sensitivity. Thus, 'mid-band' MCT detectors have a cut-off of about 600 cm^{-1}, while their sensitivity is about half that of the narrow-band detector. 'Wide-band' detectors cut off at ~ 450 cm^{-1} but are even less sensitive. Fortunately, few spectra of organic samples contain useful bands below 700 cm^{-1}, as a result, FT-IR microscopes are almost invariably equipped with narrow-band MCT detectors.

The noise equivalent power (NEP) of an infrared detector is a measure of the noise generated by the detector and is given by:

$$\mathrm{NEP} = \frac{\sqrt{A_D}}{D^*} \tag{1.1}$$

where A_D is the area of the detector element and D^* is the specific detectivity of the detector (which is typically a constant for a given wavelength, detector composition and temperature.) The greater the NEP, the lower is the sensitivity of the detector. Most detectors are specified in terms of their D* rather than their NEP. The D* of a narrow-band MCT detector is close to the value given by the background limit for infrared photons, and their performance can only be improved significantly by switching to a liquid-helium-cooled bolometer. To the present author's knowledge, the use of such a bolometer for mid-IR microspectroscopy has not been reported.

From Equation 1.1 it can be seen that the area of any detector used for infrared microspectroscopy should be as small as possible. Provided that all the radiation that passes through the sample is focused on the detector, the use of a 0.25 mm detector gives a SNR that is fourfold greater than if a 1 mm detector were used for the characterization of microsamples. For mid-IR microspectroscopy, the detector is usually a $250 \times 250\,\mu\mathrm{m}$ narrow-band MCT photoconductive detector, although some vendors do provide options for $100 \times 100\,\mu\mathrm{m}$ or even $50 \times 50\,\mu\mathrm{m}$-sized elements. As identical objectives are usually used to focus the beam onto the sample and the detector (e.g., see Figure 1.2), there is 1× magnification and the *largest* sample that can be measured with a 250 µm detector is $250 \times 250\,\mu\mathrm{m}$; however, this is rarely a significant limitation in mid-IR microspectroscopy when samples *smaller* than 250 µm are usually of interest.

The SNR of a FT-IR spectrum (i.e., the reciprocal of the noise of a 100% line measured in transmittance) is given by the following equation [15]:

$$\mathrm{SNR} = \frac{U_\nu(T)\,\Theta\,\Delta\tilde{\nu}\,D^*\,t^{-1/2}\,\xi}{A_D^{1/2}} \tag{1.2}$$

where $U_\nu(T)$ is the spectral energy density of the source radiation (W (sr cm^2 cm^{-1})), Θ is the optical throughput or *étendue* (cm^2 sr), $\Delta\tilde{\nu}$ is the resolution at which the spectrum is measured (cm^{-1}), t is the measurement time (s), D* is the specific detectivity of the detector (cm Hz$^{1/2}$ W^{-1}), ξ is the efficiency of the optics and A_D is the detector area (cm^2). Microscopes are designed to have a high optical efficiency, ξ, and a numerical aperture that gives the highest étendue, Θ, for small samples. The spectral resolution, $\Delta\tilde{\nu}$, is governed by the nature of the sample and the information required by the operator.

The data acquisition rate (sampling frequency) for mid-IR interferograms is usually equal to the frequency, f_L Hz, of the interferogram that is generated by a laser (usually a helium-neon laser at 632.8 nm) simultaneously with the infrared interferogram. f_L is equal to the product of the wavenumber of the laser and the

optical velocity (i.e., the rate of change of opd) of the interferometer. For a standard Michelson interferometer, the optical velocity is twice the mechanical velocity of the moving mirror. The scan speed is usually determined by the effect of the frequency on the signal being detected on the D* of the detector [15]. For example, the D* of the DTGS detector that is supplied as standard with most FT-IR spectrometers is greatest when the modulation frequencies of the signals in the interferogram are low. For the most efficient operation with a DTGS detector, therefore, the optical velocity of the interferometer must also be low. The typical optical velocity used in this case is 0.316 cm (opd) s^{-1}, corresponding to a 5 kHz signal from the interferogram generated by the 632.8 nm line of a He–Ne laser and hence a 5 kHz data acquisition rate. Conversely, the D* of the MCT detector is approximately constant for modulation frequencies between 1 kHz and 1 MHz, but decreases at lower modulation frequencies. Many continuous-scanning interferometers are operated at an optical velocity of 1.264 cm (opd) s^{-1}, corresponding to a 20 kHz signal from the 632.8 nm line of a He–Ne laser. In this case, the modulation frequency for 750 cm^{-1} radiation is ~950 Hz and radiation at all higher wavenumbers is modulated at a frequency greater than 1 kHz. Obviously, the D* remains relatively constant over the range at which the fastest instruments can scan (>100 kHz).

Most FT-IR spectra measured through a microscope are acquired at a resolution of 4 cm^{-1}, which requires 8K data points for each symmetric (double-sided) interferogram. If the data acquisition frequency with a He–Ne laser is 20 kHz, then the time to measure each interferogram is 0.4 s. Assuming that the mirror can be turned around fairly efficiently, this implies that about 2.5 scans can be measured per second. For mapping purposes, it is fairly common to average 16 scans before advancing the position of the microscope stage; however, the number of scans required to achieve the desired SNR will depend heavily on the size of the sample aperture employed, with smaller apertures (for higher spatial resolution) requiring many more scans, typically hundreds.

Although contemporary FT-IR spectrometers and microscopes are well matched, for spectra measured when using sample apertures that approach the diffraction limit (<20 μm) even a 30 s collection may result in a spectrum with a rather poor SNR. It may be noted that if the measurement of each spectrum takes 30 s and a 64×64 map is required at 20 μm spatial resolution, it would take over 34 h to acquire all the spectra required for the image!

At this point, it may be asked if certain parameters can be changed to decrease the measurement time to allow maps to be acquired in reasonable times. As the size of the remote aperture for most applications is smaller than 250 μm, it is valid to suggest that even smaller detectors should be installed in FT-IR microscopes, so that the SNR is optimized for samples that are 50 μm or smaller in dimension. The answer is a very practical one: it is simply very difficult to keep the beam aligned with the tighter tolerance required for the beam to be focused accurately on a detector that is smaller than 250 μm. As we will see later, the situation is different when array detectors with very small pixels are used for hyperspectral imaging.

The measurement time, t, is largely determined by the goal of the experiment. If only a few regions of the sample are of interest, then several minutes can be used for each measurement. However, if the sample is to be mapped, hundreds of spectra are often needed and the time for each should be less than 1 min if the measurement is to be completed in a reasonable time.

1.2.3 Sources for Mid-Infrared Microspectroscopy

One parameter in Equation 1.2 has not yet been discussed, namely the spectral energy density, $U_\nu(T)$. The only parameter that can lead to a significantly improved SNR is the spectral energy density of the source radiation, $U_\nu(T)$. In general, the operators of laboratory FT-IR spectrometers have little control over the source installed in their instruments. Most instruments are equipped with an incandescent silicon carbide source, such as a Globar, operating at about 1400 K. The emission characteristics of mid-IR sources are usually similar to those of a blackbody, so that it is possible to increase the spectral energy density by increasing the temperature of the source. However, increasing the temperature of a Globar often leads to cracking and the rapid degradation of electrical contacts at the end of the rod. One material that has been reported to be operable to over 1950 K is molybdenum silicide; another source that can be taken up to a temperature close to 2000 K is a homogeneous material with the chemical formula $Mo_xW_{1-x}Si_2$, which is available commercially as Kanthal Super 1900. The molybdenum and tungsten atoms are isomorphous in this chemical formula, and can thus replace each other in the same structure. However, a detailed comparison of any of these materials with a Globar with respect to infrared microspectroscopy has, to the present author's knowledge, never been reported.

Provided that samples can be removed from the laboratory, there are two alternative sources of infrared radiation that are far better than incandescent sources for mid-IR microspectroscopy, namely the synchrotron and the free electron laser (FEL) [16].

A synchrotron is a particular type of cyclic particle accelerator, or cyclotron, in which the particles are electrons. A magnetic field is used to bend the path of the electrons and an electric field is used to accelerate them. Both fields are carefully synchronized with the traveling beam of electrons. By increasing the two fields appropriately as the particles gain energy, their path can be controlled as they are accelerated. This allows the particles to be contained within a large narrow ring, with some straight sections between the bending magnets and some bent sections within the magnets giving the ring the shape of a round-cornered polygon. This shape also allows (and, in fact, requires) the use of multiple magnets to bend the particle beam. The strength of the transverse magnetic field is varied periodically by arranging magnets with alternating poles along the beam path. This array of magnets is sometimes called an undulator, or 'wiggler', because it forces the electrons in the beam to assume a sinusoidal path. The acceleration of the electrons along this path results in the release of a photon.

In a typical cyclotron, the maximum radius is quite limited as the particles start at the center and spiral outward; thus, the entire path must be a self-supporting, disc-shaped evacuated chamber. As the radius is limited, the power of the device becomes limited by the strength of the magnetic field, but synchrotrons overcome this limitation through the use of a narrow beam pipe that can be surrounded by much smaller and more tightly focused magnets. The ability of this device to accelerate particles is limited by the fact that the particles must be charged to be accelerated at all, and all charged particles under acceleration emit photons, thereby losing energy. The limiting beam energy is reached when the energy lost to the lateral acceleration required to maintain the beam path in a circle equals the energy added each cycle. More powerful accelerators are built using larger radius paths and by using more numerous and more powerful microwave cavities to accelerate the particle beam between corners.

A FEL shares the same optical property as a conventional laser; that is, the emission of a beam of coherent electromagnetic radiation that can reach high power. However, FELs use some very different operating principles than a conventional laser to form the beam. Unlike conventional lasers, which rely on bound atomic or molecular states, FELs use a relativistic electron beam as the lasing medium, which gives them the widest frequency range of any laser type, and makes many of them widely tunable, currently ranging in wavelength from microwaves to soft X-rays. In certain respects, the FEL is similar to a synchrotron. To create a FEL, a beam of electrons is accelerated to relativistic speeds. As in the operation of a synchrotron, the beam passes through a periodic, transverse magnetic field. However, in an FEL, the undulator is placed in an optical cavity, or resonator, that reflects the emitted light back and forth. The electrons become tightly bunched because of interactions with a light beam that is also passing through the undulator. The light may either be introduced from an external 'seed' laser or, more frequently, is radiation that has been generated from a previous bunch of electrons that is reflected from mirrors that form an optical cavity outside the undulator.

Viewed relativistically in the rest frame of the electron, the magnetic field can be treated as if it were a virtual photon. The collision of the electron with this virtual photon creates an actual photon by Compton scattering. Mirrors capture the released photons to generate a resonant gain, while the wavelength can be tuned over a wide range by adjusting either the energy of the electrons or the field strength. As the energy of the emitted photons is governed by the speed of the electron beam and magnetic field strength, an FEL can be tuned. Furthermore, because the resonance is specific for light of a given wavelength, the power of the beam is significantly greater than that of a synchrotron, for which broadband radiation is emitted.

What makes this device a laser is that the electron motion is in-phase with the field of the light already emitted, so that the fields add coherently. As the intensity of the emitted light depends on the square of the field, the light output is increased. In the rest frame moving along the undulator, any radiation will still move with the speed of light and pass over the electrons, allowing their motion to become synchronized. The phase of the emitted light is introduced from the outside.

Depending on the position along the undulator, the oscillation of the electrons is either in-phase or out-of-phase with the radiation introduced from the outside. The light either tries to accelerate or decelerate these electrons, thereby gaining or losing kinetic energy, and so moves faster or slower along the undulator. This causes the electrons to form bunches; when they are synchronized they will in turn emit synchronized (i.e., coherent) radiation.

Steiner *et al*. have reported the measurement of maps of octadecanephosphonic acid (OPA) molecules deposited on a microstructured aluminum oxide/gold surface using an FEL source [17]. The beam from the FEL was first passed through an interferometer to modulate the beam at a frequency of a few kilohertz. (Note that as the FEL emits monochromatic radiation, the interferometer was only used as a modulator and served no spectroscopic function.) The beam was then passed through a wire-grid polarizer and a photoelastic modulator so that the polarization was switched at a rate of 75 kHz, and then through a pinhole to be focused onto the sample with a Cassegrainian objective at an incidence angle of approximately 60°; in this way the diameter of the Airy disk (*vide infra*) was about 15 μm. Radiation that was polarized such that the electric vector was parallel to the surface was absorbed by the surface species, whereas radiation polarized such that the electric vector was perpendicular to the surface was not absorbed. The beam was collected by a second Cassegrain and then refocused at the detector. As the detector signal is passed into a lock-in amplifier referenced to the polarization modulation frequency, the interferogram was caused only by the surface species [18]. The sample was then moved in a raster fashion in order to generate a spectroscopic map that showed OPA to be attached on the aluminum oxide surface, and not to the gold. Although the attached molecules formed a highly ordered film, a lower degree of ordering was found for phosphonic acid adsorbed onto gold.

For these investigations, Steiner *et al*. measured either 40×40 or 20×20 pixels per image, with three scans being averaged for each data point. The measurement time per pixel for a single wavelength was ~5 s, with an additional 2 s for data processing; hence, the total measurement time per image for a single wavelength was 190 min for the 40×40 pixel image and 45 min for the 20×20 pixel image. Under normal conditions, the operators of the FEL require 10–20 min to change the wavelength of the FEL; thus, to measure the image at three wavelengths required at least a day.

From a spectroscopic standpoint, the main difference between a synchrotron and an FEL is that a synchrotron emits broadband radiation, while the FEL emits monochromatic radiation with several orders of magnitude higher brilliance than a synchrotron. Thus, radiation from a synchrotron can be expanded and passed into a FT-IR spectrometer, for which the interferometer and all the subsequent optics are no different from those in a conventional FT-IR spectrometer (or microspectrometer.) When a FEL is used for spectroscopy, the monochromatic radiation generated can be modulated in any appropriate manner (e.g., by a tuning fork chopper) before being passed onto the sample and detector. In principle, FELs can

be used for imaging by passing monochromatic radiation onto a focal plane array detector and measuring the signal from each pixel (*vide infra*), although such experiments have not yet been reported. The laser would then be tuned to the next wavelength of interest, and this process would be repeated for as many wavelengths as were needed to characterize the sample. This is rarely a fast process, as it usually takes several minutes to change from one wavelength to the next.

The synchrotron has an equivalent black-body temperature of 10 000 K [19]. The effective diameter of the beam from a synchrotron is typically about 100 μm; moreover, the light is emitted into a narrow range of angles, making this an almost perfect radiation source for mid-IR microspectroscopy. Not all synchtrotrons are equipped with infrared beam lines, although as the importance of the results obtained continues to increase this situation is changing. Beam time on most synchrotrons is highly prized, and potential users may often have to write a short proposal to be granted beam time. However, since FT-IR microscopes with a synchrotron source allow spectra with diffraction-limited spatial resolution and high SNR to be measured in a few seconds, many spectroscopists are starting to use the combination of synchrotron source, FT IR spectrometer and either a single-element detector or an array detector [20–23].

1.2.4 Spatial Resolution

Today, FT-IR microscopes are designed to allow the spectra of physically small samples, or regions of small samples, to be measured as quickly and easily as possible. An example of such a system is shown in Figure 1.3. On this microscope, a video image of the sample is displayed on the monitor screen immediately adjacent to the sample; this allows the position of the sample and the jaws of the aperture to be optimized prior to measurement of the spectrum. A motorized sample stage allows mapping to be readily accomplished.

The spatial resolution of a microscope is ultimately determined by diffraction of the radiation. If monochromatic radiation from a point source is passed into the microscope, then a series of concentric rings of decreasing intensity is seen at the beam focus. The Airy disk is the central bright circular region of the pattern produced by light diffracted when passing through a small circular aperture. The size of the Airy disk depends on the wavelength of the radiation and the optics of the microscope. The radius of the Airy disk is the distance between the central maximum and the first minimum of the diffraction pattern and is given by:

$$r = 0.61\frac{\lambda}{NA} \tag{1.3}$$

Here, NA is the numerical aperture, defined as:

$$NA = n\sin\theta \tag{1.4}$$

Figure 1.3 The Bruker Optics Hyperion microscope. Courtesy of Bruker Optics.

where n is the refractive index of the medium in which the optics are immersed (i.e., 1.0 for air and up to 1.56 for oils) and θ is the half-angle of the maximum cone of light that can enter or exit the condenser or objective. (Immersion optics are almost never used for infrared microspectroscopy because of absorption by the oil, but have occasionally been used to improve the spatial resolution in Raman microspectroscopy. Immersion oils have been shown to be essential in order to obtain good depth resolution with confocal Raman microscopy [24].)

Two objects are completely resolved if they are separated by $2r$, and barely resolved if they are separated by r. The latter condition is sometimes known as the *Rayleigh criterion of resolution*. The largest numerical aperture that can generally be achieved for a Cassegrainian optic is approximately 0.6, so the diffraction-limited spatial resolution is approximately equal to the wavelength of the light when $n = 1.0$.

Although it was stated that the spatial resolution of a microscope is ultimately limited by diffraction, all modes of chemical imaging employ detector elements of finite size. When the image of the pixel at the sample plane becomes the limit-

ing aperture, it can often become the limiting factor determining the ultimate spatial resolution before wavelength-limited diffraction effects become apparent. As the wavelengths of radiation across the mid-IR spectrum typically range from 2 to 14 μm, and if the pixel size at the sample plane (which is a function of native detector pixel size and overall system magnification) is larger than the wavelength being used to measure it, then the system is said to be 'pixel size-limited'. Conversely, if the wavelength of light being used to measure the sample is smaller than the pixel size at the sample plane, the system is said to be 'diffraction-limited'. This is an important – yet often misunderstood – concept. For example, the use of higher magnification objectives (e.g., 36×) results in very small images at the sample plane. However, this does not necessarily result in an improved spatial resolution, as these systems are often already diffraction-limited. Some focal plane array (FPA) imaging systems, report a pixel size of 1.1 μm when a 36× objective is used, but this is a 'waste of pixels' as the pixel size is significantly smaller than the wavelengths of light in the mid-IR; that is, the resolution is already diffraction-limited. In the example of the 36× objective providing a 1.1 μm pixel size, this spatial resolution could only really be achieved at 9000 cm^{-1}, well beyond the high wavenumber cut-off of the FPA.

In practice, even though the size of the images of the pixels at the sample plane is smaller than the wavelengths of light being used to measured the sample, the finite thickness of the sample (typically 5–20 μm) can degrade the achievable spatial resolution significantly. This effect is discussed further in Section 1.4.

While several types of microscope are commercially available for mid-IR microspectroscopy, these differ in how the sample is apertured and how the light is transferred within the microscope. The first has the simple design concept shown in Figure 1.2, namely that the beam from the interferometer is focused at the sample; thus, the sample is at an image of either the source or the Jacquinot stop (for higher-resolution FT-IR spectrometers). The beam is then refocused at the remote aperture and then again onto the detector. In the alternative design, the beam from the interferometer is passed through two apertures, one before and one after the sample, as shown schematically in Figure 1.4. This approach, which originally was called *redundant aperturing* and is now more frequently known as *dual aperturing*, provides a slightly higher spatial resolution near the diffraction limit than the single-aperture design, as shown on a theoretical basis in Figure 1.5. The second aperture serves much the same purpose as the pinhole in a confocal microscope (*vide infra*.)

Sommer and Katon [25] reported an elegant experiment that verified the improvement of spatial resolution through the use of dual aperturing. These authors mounted a free-standing polymer film at the beam focus of a microscope with dual rectangular apertures of 8×240 μm, and then measured a series of spectra as the edge of the film was moved into the beam. The spectra were measured with both apertures installed, and also with a single aperture mounted before or after the sample. By measuring the intensity of the polymer bands, it could be shown that the worst resolution was obtained when a single aperture was located after the sample. The performance for dual remote apertures and a single aperture

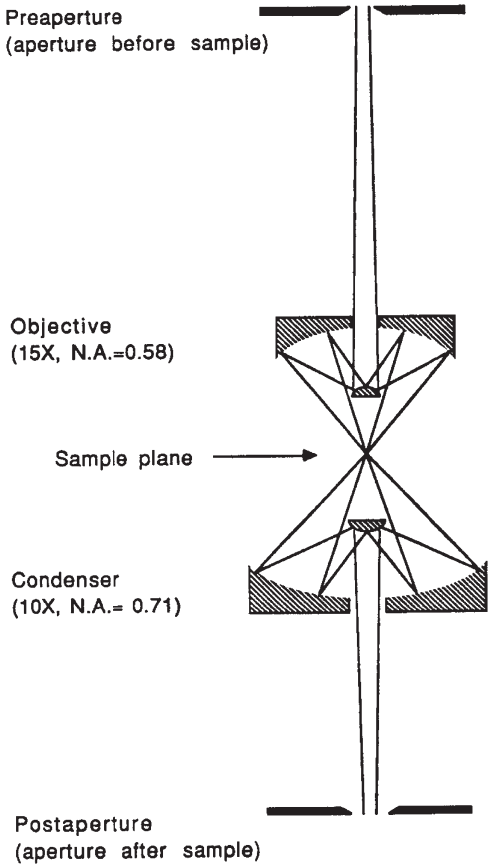

Figure 1.4 Dual-aperture microscope similar to the optics of an IRPlan microscope. Reproduced with permission from Ref. [25].

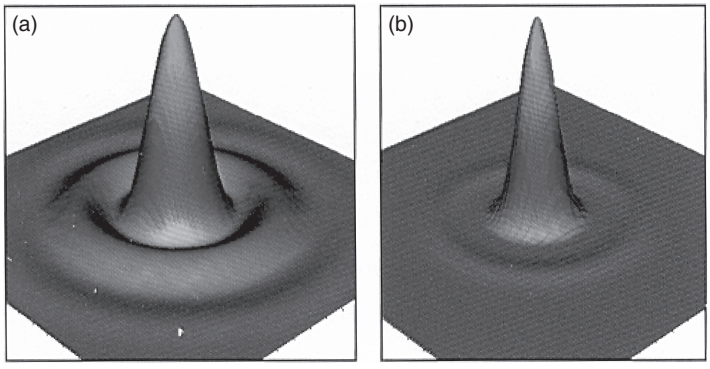

Figure 1.5 (a) Energy profile showing the diffracted radiation outside the area defined by a single aperture; (b) Corresponding profile obtained with masks located before and after the sample. Reproduced from *Infrared Fourier Transform Spectrometry* by P. R. Griffiths and J. A. de Haseth; © 2007, p. 307.

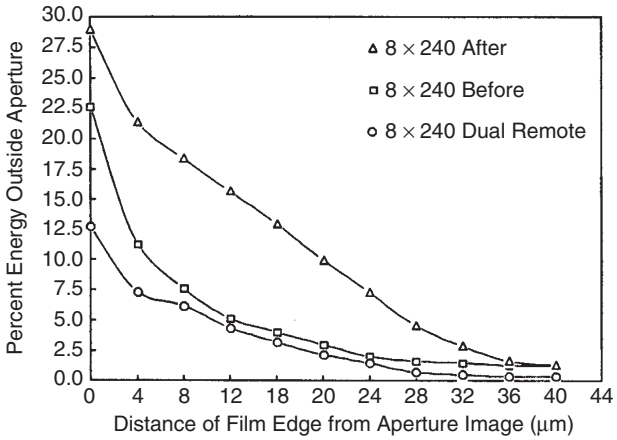

Figure 1.6 Percentage of stray energy outside the area defined by an $8 \times 240\,\mu m$ rectangular aperture for various imaging modes. Reproduced with permission from Ref. [25].

located before the sample was comparable, as shown in Figure 1.6. However, it should be noted that the dual-aperture design has the limitation that less energy reaches the detector than with the single-aperture design, so that the SNR for a given spatial resolution is decreased.

It was found that keeping the apertures of a dual-aperture microscope in alignment over a long period of use was not an easy task, especially when a high spatial resolution is desired and the apertures must be very small. Consequently, ThermoElectron devised a clever scheme to overcome this problem by using the same aperture twice, as shown in Figure 1.7.[1)] The dual-aperture concept is similar to that of a confocal microscope (*vide infra*; Section 1.5). Both, the dual-aperture design and confocal microscopes preclude imaging measurements, however, because in order to image a sample all regions of that sample which are of interest must be completely illuminated by the source radiation, while the detector pixels serve the purpose of the remote aperture that would normally be located after the sample. The dual-aperture system is ideally suited to mapping measurements with diffraction-limited spatial resolution, in which case a source of very high brightness such as a synchrotron is needed.

The manufacturers of infrared microscopes are split almost evenly between those that produce 'infinity-corrected' and those producing 'non-infinity-corrected' microscopes. Infinity correction effectively refers to a collimation of the beam throughout the microscope (other than at the condenser and objective outputs), and is frequently used in research-grade optical microscopes. Despite the added

1) Nicolet Corporation made its first FT-IR spectrometer in 1971 and became the market leader shortly afterwards. In 1995, ThermoElectron Corporation purchased Nicolet and dropped the Nicolet name. In 2006, Thermo Electron purchased Fisher Scientific and the corporation is now known as Thermo-Fisher.

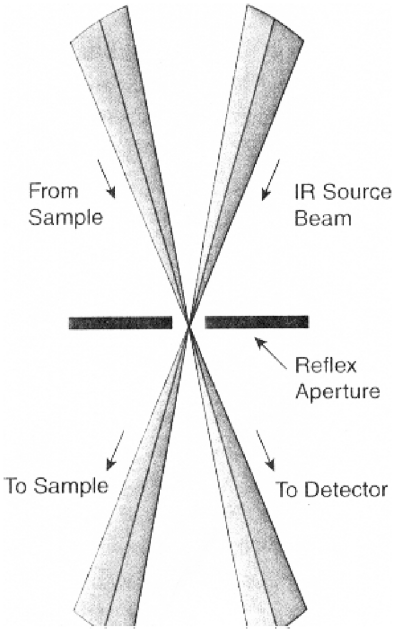

Figure 1.7 Dual confocal aperturing achieved with a single physical aperture. Reproduced from Infrared Fourier Transform Spectrometry by P. R. Griffiths and J. A. de Haseth; © 2007, p. 307.

complexity in microscope design, 'infinity correction' provides for added flexibility in the choice of 'off-the-shelf' visible objectives (as most are for infinity-corrected systems), and also in that filters and other optical components can be placed anywhere where the beam is collimated. Infinity correction can also provide for improved image clarity and focus. Non-infinity-corrected microscopes (otherwise known as 'finite tube length' microscopes), although less complex in design, are limited in terms of available options, such as other objectives, the placement of filters and other optical components, and sometimes also in the quality of the images in terms of clarity and focus. For those microscopes that are most commonly used in conjunction with FT-IR spectrometers, Varian and Thermo-Fisher employ the infinity-corrected type, while Bruker and PerkinElmer use non-infinity-corrected optics.

1.2.5
Transmission Microspectroscopy

Occasionally, transmission spectra of small inhomogeneous samples show the presence of artifacts. For example, the effect of scattering may cause symmetrical bands to lose their symmetry. Instead of having the symmetric shape of the absorption index spectrum, the stronger bands begin to take on the appearance of the

refractive index spectrum (this phenomenon is sometimes called the Christiansen effect [26]). Romeo *et al.* [27, 28] observed a second effect caused by light scattering while measuring the infrared spectrum of whole cells using FT-IR microspectroscopy. These authors showed that light scattering by the nucleus introduces a broad undulating spectral feature into the baseline of the spectrum, which they attributed to Mie-type scattering by the cell nucleus. Dielectric spheres are known to scatter electromagnetic radiation if the wavelength of the light is comparable to the sphere's size. The theory of this scattering process was first described (on a theoretical basis) by Mie [29], and has been nicely summarized by Romeo *et al.* [27, 28]. The same effect is visible in Raman spectroscopy, causing baseline ripples and perturbation of band intensities. In Raman spectroscopy the effect is sometimes termed 'morphology-dependent resonance'.

Mie theory assumes a spherical scattering particle in the field of a plane electromagnetic wave. The scattering cross-section Q_{sca} of a dielectric sphere interacting with a plane electromagnetic wave is given by a series expansion of the size parameter, ρ, and complicated expressions in the half-integer order Bessel (Ricatti–Bessel) functions of the first type and their complex equivalents (Hankel functions). The size parameter ρ is defined by

$$\rho = 2\pi r\, m_o/\lambda \tag{1.5}$$

where r is the radius of the sphere, λ the wavelength of the light, and m_o the ratio of the refractive indices between the sphere and the surroundings. The Bessel functions account for the undulating wavelength dependence of Mie scattering.

The angular dependence of Mie scattering is given by series expansions in the Legendre polynomials and their derivatives with respect to the scattering angle. While the exact solution of this problem is rather complex, Diem's group also used an approximate formula, which was first reported by Walstra [30]:

$$Q_{sca} = 2 - (4/\rho)\sin\rho + (4/\rho^2)(1-\cos\rho) \tag{1.6}$$

where ρ is the size factor as defined above. This approximation reproduces the rigorous calculation to within 1%, and matches the spectra remarkably well. By using the approximate calculations, Romeo *et al.* were able to model the Mie scattering background satisfactorily, and corrected the distorted spectra by subtracting the modeled Mie background.

1.2.6
Attenuated Total Reflection Microspectroscopy

It can be seen from Equations 1.2 and 1.3 that the spatial resolution of infrared microspectroscopy can be improved by immersing the sample in a medium of high refractive index. This exactly what is done in attenuated total reflection (ATR) spectroscopy using a single-reflection hemispherical internal reflection element (IRE). For example, if a germanium ($n = 4.0$) hemispherical IRE is used, not only

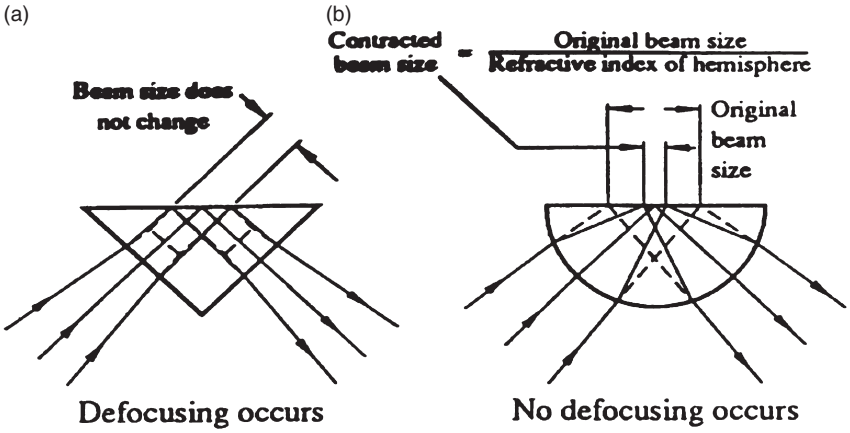

Figure 1.8 Beam focusing through (a) prismatic and (b) hemispherical internal reflection elements.

is an increase in the numerical aperture obtained (because of the increased refractive index of Ge), but the outer ray angle of incidence (which defines *NA*) is also increased, as the light is refracted inwards. The difference between the focusing that occurs with a triangular prism and a hemispherical IRE is seen in Figure 1.8a and b.

The first ATR accessory to make use of a single-reflection IRE with approximately hemispherical geometry was the Split Pea (Harrick Scientific), the usual image size of which is about 250 µm when used with a germanium IRE. Although germanium has the highest refractive index of infrared transparent materials (and therefore gives the greatest demagnification), it has the great disadvantage in that it is not transparent to visible light. As a result, sample alignment in some of the earlier devices was quite tricky. Since the introduction of the Split Pea, a number of analogous accessories have been introduced for ATR microspectroscopy, including several that have been explicitly designed to replace the objective in a standard infrared microscope. The Bruker Optics Hyperion, as shown in Figures 1.9 and 1.10, is just one example of a microscope designed for FT-IR microspectroscopy; analogous systems are available from a number of different vendors. Several manufacturers have designed accessories where the sample can be aligned without being in contact with the IRE. When the appropriate region has been selected, the IRE is moved into place. With the Bruker Hyperion, the tip of the internal reflection element is 100 µm in linear dimension to achieve high spatial resolution; this instrument is equipped with an electronic pressure sensor to ensure good contact with the sample, which is particularly important for mapping by ATR microscopy. The IRE is spring-loaded to avoid damage, and there are five different pressure steps to allow optimal contact for hard and soft samples.

Like germanium, silicon also has a fairly high refractive index ($n = 3.4$). Silicon is rarely used for the fabrication of large IREs (for which the optical path may be

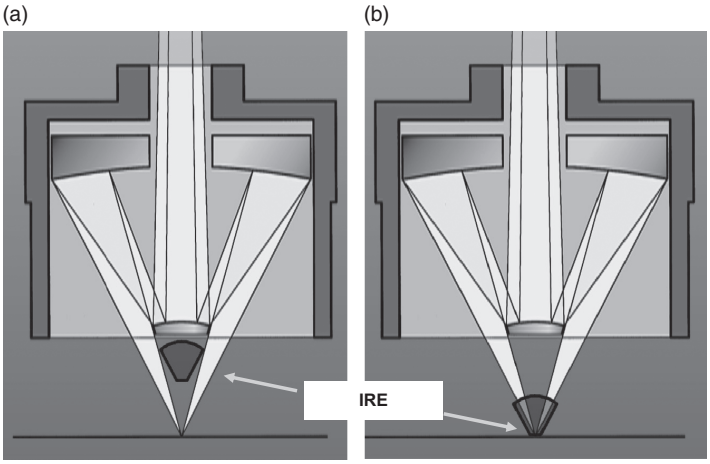

Figure 1.9 Optical schematic of the Bruker Optics ATR objective used in (a) alignment mode and (b) spectral acquisition mode. Illustration courtesy of Bruker Optics.

Figure 1.10 Photograph of the Bruker Optics ATR objective. Illustration courtesy of Bruker Optics.

several centimeters) because the presence of trace impurities leads to excessive absorption of the radiation below about 1200 cm^{-1}. With the very short path through the IRE installed in a microscope objective, however, this is no longer a problem. Thus, either silicon or germanium can be used productively as the IRE in an ATR objective.

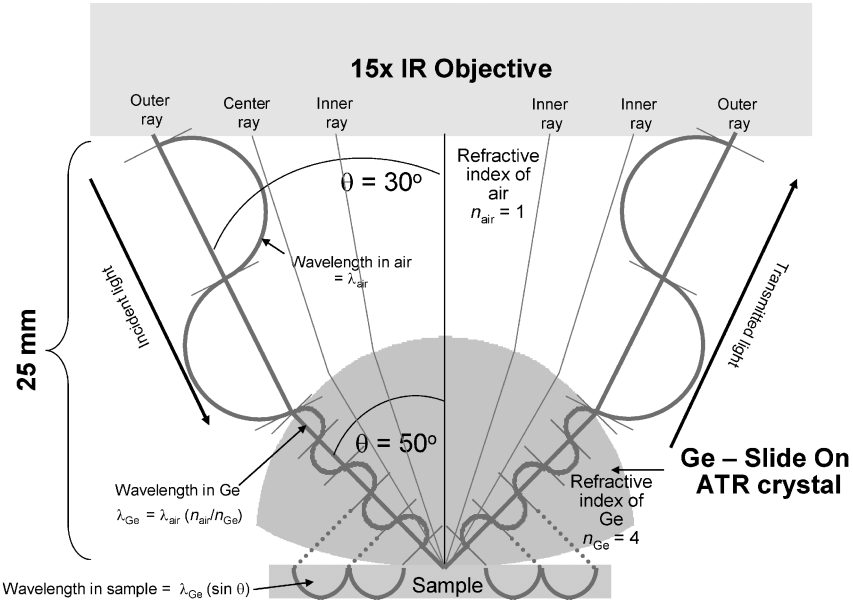

Figure 1.11 Schematic of Varian's Ge slide-on ATR objective, showing how the spatial resolution is enhanced by increasing the refraction index of the medium to 4 with Ge and increasing the outer ray angle of incidence to 50°, resulting in a numerical aperture of 3.1. Illustration courtesy of Varian Corporation.

The increase in numerical aperture achieved through the use of hemispherical IREs can be seen more quantitatively by considering the design of Varian's slide-on Ge ATR accessory, shown in Figure 1.11. On refraction, the outer ray angle which is normally 30° (for a *NA* of 0.5) is increased to 50° after refraction through the Ge IRE. In the Varian design, the underside of the hemisphere (which is in contact with the sample) has a relatively large radius of curvature, such that over the field-of-view of the IRE (~100 × 100 μm), it is effectively flat.

1.3 Raman Microspectroscopy and Mapping

1.3.1 Introduction to Raman Microspectroscopy

In principle, Raman microspectroscopy is attractive because the practical diffraction limit is on the order of the excitation wavelength, which is about 10-fold smaller for Raman spectroscopy with a visible laser than for mid-IR spectroscopy. It is therefore possible to focus visible or NIR laser light to much smaller spot

sizes (~1 μm or less) than may be examined by mid-IR radiation. Until the mid 1980s, however, Raman spectrometry was a time-consuming and relatively unpopular technique for the characterization of both macro- and micro-samples for the following reasons:

- The intensities of strong bands in Raman spectra are usually at least 10^8-fold weaker than the intensity of the incident monochromatic beam.
- When photomultiplier tubes (PMTs) were used for the detection of Raman spectra, high-power gas lasers (e.g., Ar^+) were required to yield enough photons for the measurement of Raman spectra in less than 1 h; the power supplies for the early versions of these lasers generated so much heat that they often required water cooling.
- Inefficient double and triple monochromators were required to eliminate stray light from the Rayleigh line.
- No multiplex or multichannel technique was available for the measurement of Raman spectra; hence, the instruments were based on scanning monochromators with a single PMT detector.
- Many 'real-world' samples fluoresce when illuminated with visible light, especially green light from a frequency-doubled neodymium-doped yttrium aluminum garnet (Nd-YAG) laser at 532 nm or from an argon ion laser at 488 or 514.5 nm.

Although nothing can be done to make the Raman cross-section of vibrational bands any greater without the application of techniques such as resonance Raman spectroscopy or surface-enhanced Raman scattering, several important technological developments have led to the design of today's truly powerful Raman spectrometers. These included (in no particular historical order) the development of:

- Highly efficient notch filters that eliminate the Rayleigh line and transmit both the Stokes- and anti-Stokes Raman bands, or edge filters that transmit only the Stokes Raman bands and block all shorter-wavelength radiation.
- Small, efficient single monochromators based on concave holographic gratings, transmission holographic gratings or standard Czerny–Turner monochromators in combination with a notch filter.
- 'Scientific' CCD array detectors with quantum efficiencies close to 100%.
- Visible lasers operating at much lower input power than the earlier gas lasers; the most important of these is the He–Ne laser (632.8 nm), while argon ion (488.0 and 514.5 nm) and krypton lasers (647.1, 568.2 and 530.9 nm) are also useful for Raman spectroscopy.
- Diode lasers emitting at 785 and 840 nm, which minimize fluorescence and are still compatible with silicon-based CCD detectors over much of the Raman spectrum.

- Diode-pumped Nd:YAG lasers emitting at 1064 nm: with a laser operating at this long wavelength, fluorescence from the sample is often minimized and sometimes eliminated.
- The frequency-doubled Nd:YAG laser emitting at 532 nm.
- The recent development of blue/green diode lasers operating at, for example, 472 nm.
- FT Raman spectrometry, which was needed because the Raman spectrum-generated 1064 nm radiation was at too long a wavelength for silicon-based CCD detectors.
- Efficient fiber-optic probes.

The first report of the design and testing of an FT-Raman spectrometer was by Hirschfeld and Chase in 1986 [31], and this became available commercially during the following year. With these instruments, the sample is illuminated with 1064-nm radiation from a Nd:YAG laser, while the Rayleigh- and Raman-scattered light is modulated by a two-beam interferometer. After removal of the Rayleigh-scattered radiation by a notch or edge filter, the Raman interferogram is detected using either an indium gallium arsenide (InGaAs) or germanium detector. Within another year, however, Raman spectrometers based on a polychromator and a CCD array detector were also brought onto the market. These instruments were compatible with essentially any laser that led to the generation of a Raman spectrum at shorter wavelength than the 1100 nm cut-off of silicon-based CCD detectors. Thus, instruments became available with, *inter alia*, a doubled Nd:YAG laser (532 nm), a low-power He–Ne laser (632.8 nm) or NIR diode lasers, of which 785 nm and 840 nm were the most common wavelengths. Neither of these diode lasers is capable of measuring the complete Raman spectrum. For example, if an 840 nm (11 900 cm^{-1}) diode laser is used, the Raman spectrum beyond about 2500 cm^{-1} is beyond the cut-off of a silicon CCD.

These FT-Raman and CCD-Raman spectrometers revolutionized Raman spectroscopy such that, within the space of about five years, about ten different Raman spectrometers based on multiplex and multichannel technologies had been introduced commercially [32, 33]. Several of the CCD-Raman spectrometers were either designed for, or could be readily modified for, microspectroscopy. Although FT-Raman microspectrometers have been reported (e.g., Ref. [34]), they have not proved very popular for three reasons:

- Safety: the 1064 nm beam of a FT-Raman spectrometer is high powered, completely invisible and quite dangerous.
- When the beam from a Nd:YAG laser is focused on a sample that absorbs 1064 nm radiation, even the weakest absorption band will cause significant heating. In fact, it is quite common for samples to ignite, or at least to generate background blackbody radiation.

- FT-Raman spectroscopy is relatively insensitive compared to dispersive Raman spectroscopy, due to the longer wavelength of excitation and the poor noise performance of detectors in the NIR. This means that FT-Raman microscopes lack the sensitivity to analyze small samples unless high laser powers are employed, which leads to the problems noted above.

In practice, therefore, CCD-Raman spectrometers have proved to be far more successful for Raman microspectroscopy than FT-Raman spectrometers, and most instruments are based on this concept.

Raman microspectroscopy was not a completely new concept. In 1966, Delhaye and Migeon [35] showed that a laser beam could be tightly focused at a sample, and that Raman-scattered light could be collected and transferred to a spectrometer, with minimal loss. Their calculations showed that the increased irradiance more than compensated for the decrease in the size of the irradiated volume. The first Raman microscope was reported by Delhaye and Dhamelincourt in 1975 [36], and an instrument based on these principles (the MOLE) was introduced by Jobin Yvon at about the same time. However, the optical scheme used for imaging, which employed global illumination, was inefficient and it was not until the advent of CCD-Raman spectrometers that the advantages of Raman microscopy became apparent.

Arguably the most important advantage of many microscopes used for Raman microspectroscopy is the fact that they have a confocal design. In such a design (see Figure 1.12) the laser beam is first focused on a small aperture (to clean up the beam profile and present a diffraction-limited source), and then refocused by an objective lens with a large numerical aperture onto a small (ideally diffraction-limited) focal volume within the sample. A mixture of the Raman- and Rayleigh-scattered light from the illuminated spot is then collected by the objective lens. The high *NA* of these optics allows the light to be collected over a solid angle of almost a full hemisphere. An objective with a *NA*-value of 0.95 collects about 70% of the radiation emitted over 2π steradians. A dichroic beamsplitter (typically a

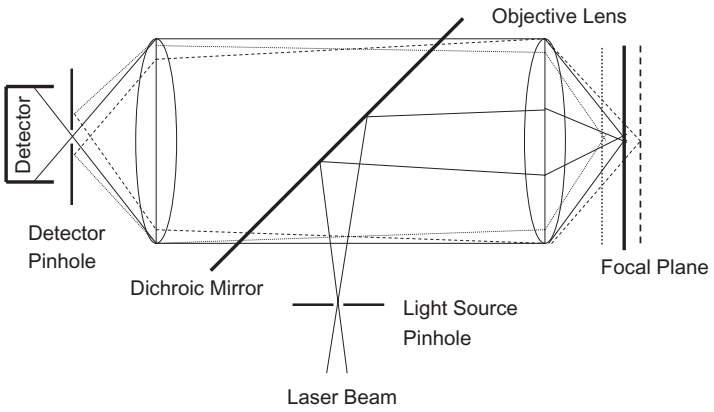

Figure 1.12 Schematic representation of the optics of a confocal microscope.

notch filter or an edge filter) reflects the radiation from the Rayleigh line and transmits the Stokes-shifted Raman-scattered radiation at longer wavelength. After passing through a pinhole, the Raman-scattered light is passed into the monochromator and the intensity at each wavelength is measured. The small spot enables the image to be transferred to the spectrometer though the narrow (typically ca. 100 µm) entrance slit with a minimal loss in energy. Today, several Raman microspectrometers employ confocal optics, which provide the capability to produce blur-free images of thick samples at various depths. It may be noted, however, that spherical aberration limits sampling with diffraction-limited resolution at depths much greater than 10 µm.

As seen in Figure 1.12, the detector pinhole obstructs the so-called out-of-focus (or out-of-plane) light, especially light from adjacent spatial regions and fluorescent emission not originating from the focal plane of the objective lens. Light rays from below the focal plane come to a focus before reaching the detector pinhole, and then expand out so that most of the rays are physically blocked from reaching the detector by the pinhole. In the same way, light from above the focal plane is focused behind the detector pinhole, so that most of this light is also vignetted by the pinhole and is not detected. However, all the light from the illuminated focus (solid lines) is imaged at the pinhole and passed to the detector. The detected light originating from an illuminated volume element within the specimen is then focused on the entrance slit of a polychromator and the spectrum measured using a CCD detector. As the out-of-focus rays from above and below the focal plane are largely removed, sharper images are measured than can be acquired from conventional (non-confocal) microscopy techniques. Mapping is accomplished by moving the sample by small amounts after each spectrum has been recorded.

Several modes of operation are available in state-of-the-art confocal Raman microspectroscopy, including the measurement of samples with a spatial resolution of less than 1 µm, depth profiling and line mapping. LaPlant and Ben-Amotz have provided a detailed description of the design and construction of a confocal Raman microspectrometer [37], and several instruments are now available commercially. In the case of the HORIBA Jobin Yvon LabRAM ARAMIS Raman spectrometer (see Figure 1.13), up to four lasers (three internal, one external), four gratings and four notch filters may be automatically switched in order to optimize the performance for a given sample, as illustrated in Figure 1.14. While not every sample is an efficient Raman scatterer, this instrument ensures that many types of sample can be routinely mapped using fast point acquisitions.

Several companies, including Horiba, Renishaw and Witec, market Raman spectrometers with confocal optical configurations. The WITec alpha300 R confocal Raman microscope differs from other confocal Raman microspectrometers in that it has been designed especially for fast microspectroscopy. The data acquisition time for an entire spectrum can be less than 1 ms, which allows Raman mapping of over 10 000 spectra in less than one minute when the Raman signal is adequate. These data sets can already be evaluated during data acquisition by using filters. For example, the integrated intensities of certain bands of interest may be calculated or the position or full width at half maximum of the bands may

Figure 1.13 The HORIBA Jobin Yvon LabRAM ARAMIS Raman spectrometer. Illustration courtesy of Horiba Jobin-Yvon Corporation.

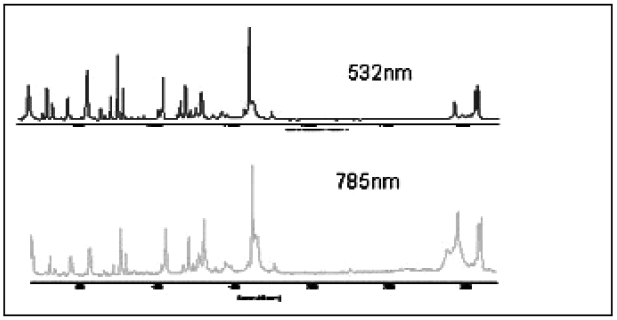

Figure 1.14 Spectra of aspirin measured with seconds of each other using a frequency-doubled Nd:YAG laser (532 nm) and a semiconductor diode laser (785 nm). Illustration courtesy of Horiba Jobin-Yvon Corporation.

be evaluated. Band fitting to Gaussian or Lorenzian shapes, as well as various other fitting algorithms, can also be applied to the data set. By using these filters, several three-dimensional (3-D) data sets that can be displayed as images are created from the four-dimensional hyperspectral data.

The WITec alpha300 R confocal Raman microscope can be upgraded to perform atomic force microscopy (AFM), tip-enhanced Raman spectrometry and near-field scanning optical microscopy, and is arguably the most versatile instrument for Raman microspectroscopy available today.

1.3.2 CCD Detectors

The quantum efficiency of contemporary array detectors can be remarkably high – in excess of 90% in the case of back-illuminated CCDs. The two main sources of noise for CCD cameras are:

- A dark current, which is largely caused by thermal emission and is usually reduced to a negligibly low level by thermoelectrically cooling the detector below –60 °C.
- Readout noise, which is the number of electrons introduced per pixel into the final signal upon the readout of the device and is caused by: (i) a lack of repeatability of the conversion from an analogue signal to a digital number; and (ii) the introduction of spurious electrons into the camera electronics, leading to unwanted random fluctuations in the output. Readout noise, which is usually given in terms of electrons, is dependent on the readout rate; typical values are 5–10 electrons for a 50 kHz readout rate to ~30 electrons for a 2.5 MHz readout rate.

The combination of these two random effects produces an uncertainty in the final output value for each pixel. In the output of the CCD image, readout noise is added into every pixel each time the array is read out. This means that a CCD with a readout noise of 30 electrons will, on average, contain 30 extra electrons of charge in each pixel upon readout. As a consequence, CCDs with a high readout noise (more than 80–100 electrons) are not very good to use if a sequence of short exposure frames is co-added instead of using one long exposure. However, for modern scientific CCDs, readout noise values are very low, in the range of 10 electrons per pixel per read or less. Ideally, the limiting noise source in any Raman spectrometer should be photon shot noise. Because photons follow Poisson statistics, for a given signal the uncertainty is the square root of the signals in electrons. In this case, the SNR of many Raman spectra can be remarkably high, even though the signal is so low. For example, even if only 100 photons are detected (converted to electrons), the SNR is still 10 – provided that the only noise source is photon shot noise.

For Raman mapping measurements, the readout time per pixel must be very short. For example, if an image consisting of 128 pixels per line and 128 lines is acquired with an integration time of 1 s per pixel, then the total acquisition time will be a little over 4.5 h. Reducing the readout time to 100 ms per pixel decreases the measurement time to 27 min. A further 10-fold reduction in the readout rate decreases the acquisition time to less than 3 min. The latter situation would allow hundreds of images to be acquired per day, instead of just one or two. Unfortunately, this condition is not readily achievable in practice because the faster the readout time of the detector electronics, the noisier is the readout amplifier.

Hollricher and Ibach [38] have described how the SNR of Raman spectra can be increased through the use of an electron multiplying CCD (EMCCD). This device is a normal CCD with an additional readout register that is driven with a significantly higher clock voltage than a normal CCD readout register. The effect of the high clock voltage is to effect an electron multiplication through impact ionization. In practice, the gain may be increased by a factor of up to 1000 in this way, so that the photon shot noise is always much greater than the readout noise. The SNR of the signal from the CH_2 stretching band of poly(methyl methacrylate) (PMMA) is shown as a function of the gain in Figure 1.15. The improved SNR allows superb

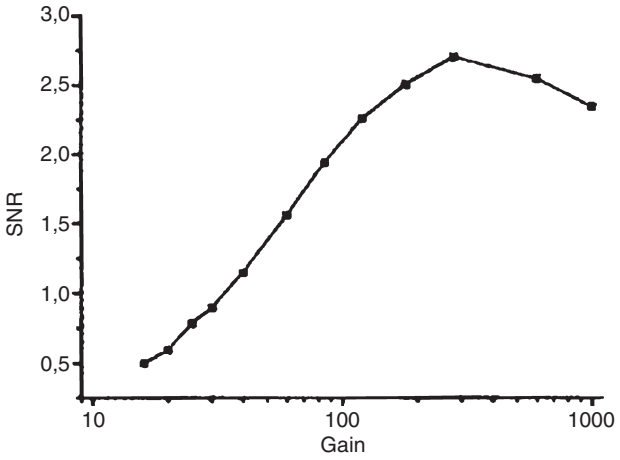

Figure 1.15 Signal-to-noise ratio of the CH_2 symmetric stretching band of PMMA plotted against the gain of the EMCCD. Reproduced with permission from Ref. [38].

images to be acquired from Raman mapping experiments in a remarkably short time. For example, a 200×200 pixel color-coded image of a 7.1 nm-thick layer of PMMA contaminated with 4.2 nm-diameter fibers acquired with a WITec alpha300R confocal Raman microscope is shown in Figure 1.16. The integration time was 7 ms per spectrum, and the total acquisition time 5.4 min. This fast response makes it feasible to map relatively large areas in minutes or hours, and is critical for practical mapping applications.

Another source of 'noise' in spectra measured using a CCD is caused by the pixel-to-pixel variation in the quantum efficiency of neighboring pixels. This variation can be corrected by illuminating the detector array with a uniform light source and measuring the signal from each pixel. Once the relative response of each pixel has been determined, a correction known as a *flat field correction* can be applied.

Despite all efforts to minimize the noise in Raman spectra measured in the short times needed for mapping measurements, it is rare that the spectroscopist would not be more satisfied if the SNR were higher. Cai *et al.* [39] reported a more powerful way of reducing the noise in Raman spectra a below that achievable by Savitzky–Golay smoothing with minimal band broadening [40]. In their approach, multiresolution wavelet transformation and block thresholding was used to both suppress the background caused by fluorescence and to reduce the noise without a significant loss in spectral resolution.

1.3.3 Spatial Resolution

For diffraction-limited microscopy, it may be thought that the image should be focused on the CCD such that the Airy disk fills one pixel. However, Adar *et al.* [41]

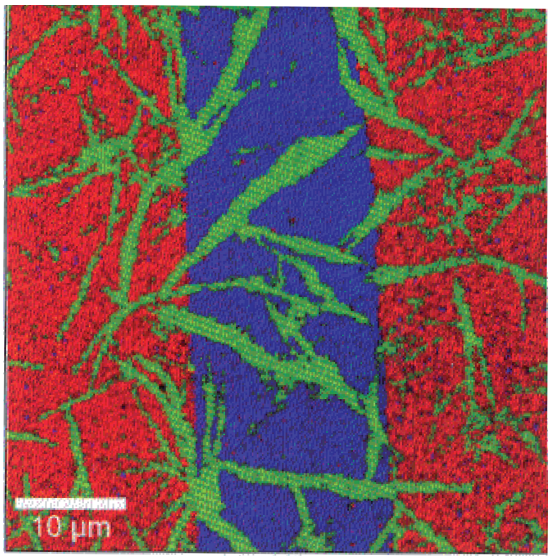

Figure 1.16 Color-coded confocal Raman map of a 7.1 nm-thick PMMA layer (red) and a 4.2 nm contaminant layer (green) on glass (blue). The map was computed from 200 × 200 spectra, with an integration time of 7 ms per spectrum, for a total acquisition time of 5.4 min. Reproduced with permission from Ref. [38].

demonstrated that image quality could be improved significantly if the sample step is much smaller than the spatial resolution of the measurement. As an example, Figure 1.17a shows the Raman map of an 8 µm polystyrene bead on a silicon substrate recorded with a 100× objective with steps of 1.0, 0.5 and 0.1 µm. The visual image recorded through a standard optical microscope is shown for comparison. Clearly, reconstructing the image from data taken with steps smaller than the resolution given by the Rayleigh criterion gives a higher quality Raman image.

The strength of the objective is, of course, also important, as it controls the numerical aperture. Figure 1.18a shows Raman maps of five 5.18 µm polystyrene spheres recorded with 100×, 50× and 20× objectives, with the increment between data points being 0.2 µm; Figure 1.18b shows the line profiles across the two beads at the top right of these images.

Information can also be collected from different focal planes by raising or lowering the microscope stage. The computer can generate a 3-D picture of a specimen by assembling a stack of these 2-D images from successive focal planes. Some care is needed in the interpretation of the results obtained by depth profiling with a confocal Raman microscope, however. For example, Everall *et al.* [24] have shown that when using metallurgical objectives, which are typically supplied as standard with confocal Raman microscopes, the focus is both much deeper than might be first thought, and is also blurred due to spherical aberration (see Figure 1.19). Even

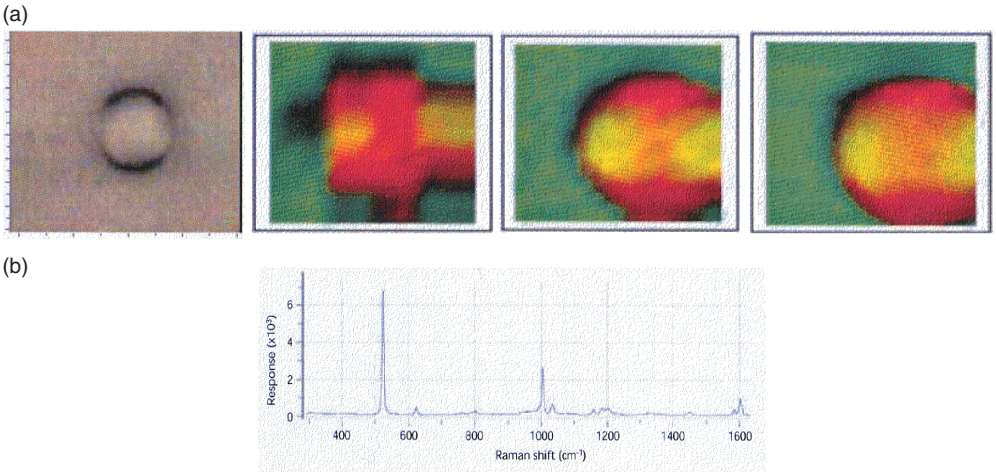

Figure 1.17 (a) Visual image of a 1 µm-diameter polystyrene bead. The lower images show Raman images of the bead, recorded with a 100× (*NA* = 0.95) infinity-corrected microscope objective at increments of (left to right) 1.0, 0.5 and 0.1 µm per step, respectively; (b) Raman spectrum measured from the center of one of these beads. Reproduced with permission from Ref. [41].

in the absence of spherical aberration, Everall has shown that bands originating from sample regions far above and below the optimum focal plane can still contribute significantly to the spectrum [42]. He demonstrated this by investigating the Raman spectra of a 20 µm-thick layer of polyethylene (PE) over a 100 µm-thick sheet of poly(ethylene terephthalate) (PET). The spectra measured at different depths, including locating the focus 10 µm above the sample, are shown in Figure 1.20. It is clear that signals from the PET contribute significantly to the spectrum, even when focused in or well above the PE. Everall demonstrated a similar effect when scanning laterally across the same sample. These results were found because, for every point within the entire illuminated volume of a transparent sample (not just the beam waist), there are some rays that can reach the detector. When all of these paths are added together, there can be a significant signal originating from those parts of the sample that are out of focus. Macdonald and Vaughn have developed a simple mathematical model to quantify the contribution of 'out of focus' regions of the sample [43].

1.3.4
Tip-Enhanced Raman Spectroscopy

By using the techniques discussed in the previous sections of this chapter, it can be seen that the spatial resolution achievable by infrared or Raman microspectroscopy is governed by the diffraction limit shown in Equation 1.3. It is possible to

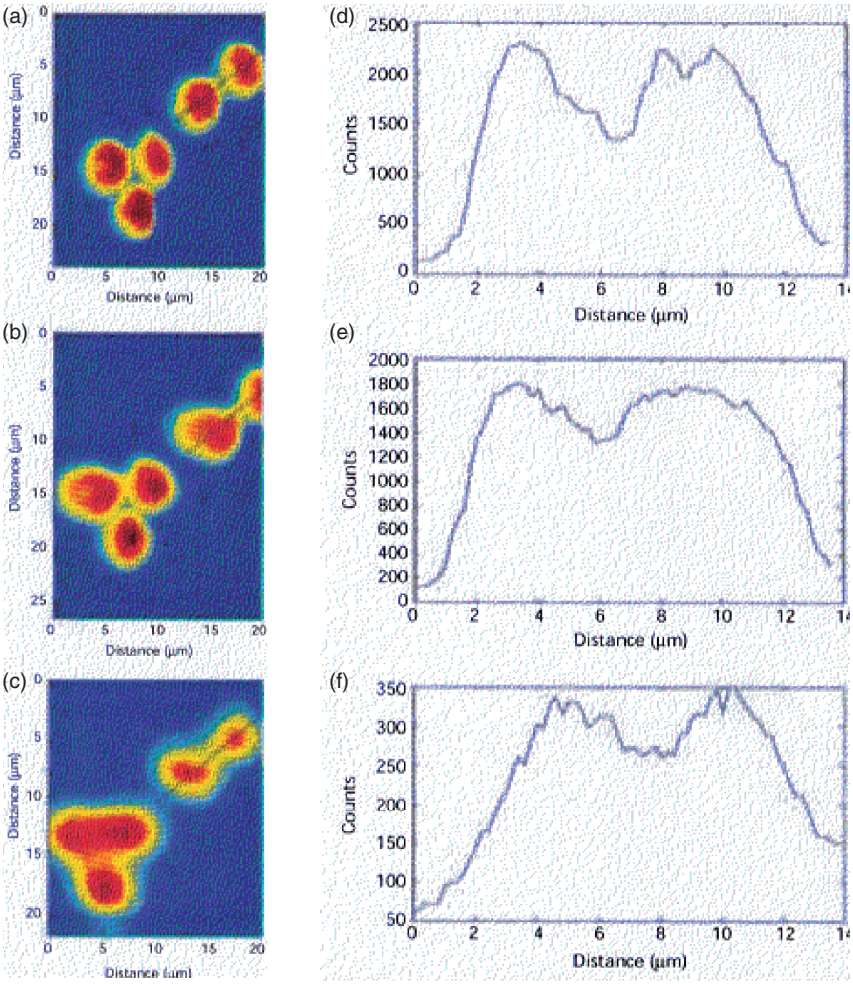

Figure 1.18 (a–c) Raman maps of 5.18 μm-diameter polystyrene beads recorded with 100×, 50× and 20× objectives, respectively. Increments between data points were 0.2 μm for all three images; (d–f) Line profiles of the two beads at the upper right in panels (a–c).Reproduced with permission from Ref. [41].

improve on the diffraction limit by near-field scanning optical microscopy (NSOM), although most of the vibrational NSOM techniques are currently in the developmental stage (see Chapter 2). However, there is one technique – known as tip-enhanced Raman spectroscopy (TERS) – whereby the spatial resolution of Raman spectroscopy can be reduced significantly below the diffraction limit [44]. TERS is a hybrid system that combines the nanometer resolution afforded by scanning probe microscopy (e.g., AFM) with the molecular specificity of surface-enhanced

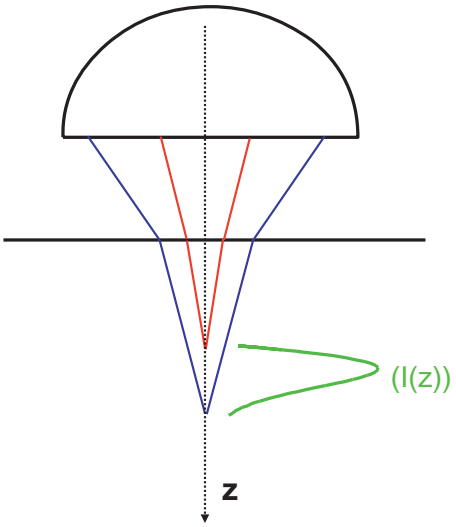

Figure 1.19 Schematic diagram showing how the effect of refraction leads to an increase in the depth of field for Raman microscopy. Illustration courtesy of Dr Neil Everall, Measurement Science Group, Intertek Corporation.

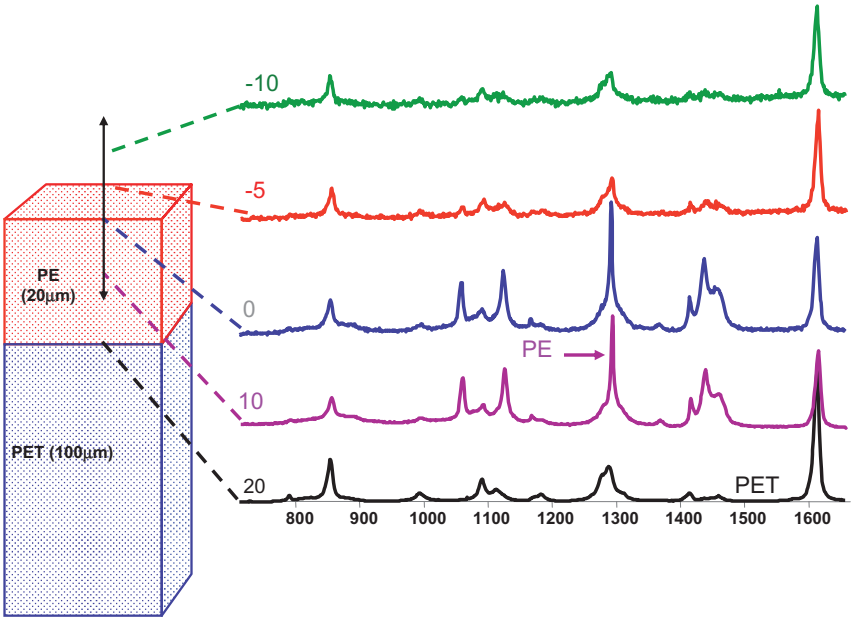

Figure 1.20 Spectra measured by raising the level of a polymer laminate sample consisting of a 100 μm-thick layer of poly(ethylene terephthalate) (PET) under a 20 μm-thick layer of poly(ethylene) (PE). The strongest bands in the Raman spectra of PE and PET are marked with arrows. Illustration courtesy of Dr Neil Everall, Measurement Science Group, Intertek Corporation.

Raman scattering (SERS). It is well known that the Raman spectrum of species with a few nanometers of roughened silver or gold surfaces is enhanced by at least four orders of magnitude. The primary enhancement in SERS arises from the electric field of the radiation being greatly increased because of resonance between the wavelength of the illumination laser and the nearby Raman signals and the wavelengths of the surface plasmon resonance of the metal nanostructures, λ_{SPR}.

It has been shown that localized plasmon polaritons in the region of sharp metal tips act in an analogous fashion, giving rise to TERS. In one mode of operation, TERS employs a sharp metal tip, which is illuminated from the outside to create a localized light source [45]. Alternatively, silver nanoparticles have been deposited on silica or titania surfaces and a silicon tip is used [46, 47]. That these tips are not easy to prepare most likely accounts for the fact that TERS is not yet widely used. Nonetheless, preliminary results have indicated the feasibility of detecting and characterizing single molecules [45] with atomic site sensitivity [48]. The investigation of bacterial surfaces [49] and single-walled carbon nanotubes [50] has also recently been reported. Although these early results are very promising, TERS is not yet widely used and will not be described in any great depth in this chapter (although a more detailed account can be found in Chapter 2).

1.4 Near-Infrared Hyperspectral Imaging

Following the above introduction to the types of microscopes used for single-point sampling and sample mapping, the instrumentation used for hyperspectral imaging by vibrational spectrometry will now be described. NIR imaging instruments will be introduced first, as these are the simplest in design. Raman imaging spectrometers will then be discussed, as these bear considerable similarity to their NIR counterparts. The instrumentation for mid-IR imaging will be described subsequently, as their operating principles are somewhat different to those of NIR and Raman imaging systems. Finally, terahertz imaging, which is based on a completely different principle to any of the other types of imaging instruments will be introduced.

Perhaps the simplest type of instrument for NIR hyperspectral imaging spectrometer is that originally developed by Spectral Dimensions, Inc. (Olney, MD, USA, now Malvern Instruments.) In this instrument, the radiation from a broadband source of NIR radiation (a simple tungsten or quartz–tungsten–halogen lamp) is passed through a liquid crystal tunable filter (LCTF) so that a narrow region of the NIR spectrum is isolated. A typical LCTF is constructed from an interwoven stack of Lyot stages (linear polarizers and liquid-crystal variable retarders mounted on birefringent quartz crystals), usually mounted in a temperature-controlled housing. A single Lyot stage of an LCTF system is shown in Figure 1.21. Varying the voltage applied to the liquid crystals shifts the pass band in less than 1 ms, without any mechanical motion or vibration of the optics. Thus, the filter can be tuned an almost infinite number of times as there is no wear and tear.

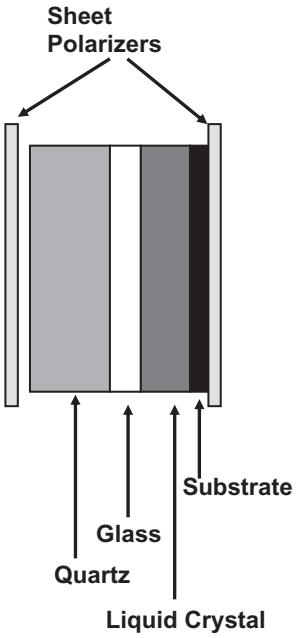

Figure 1.21 A typical Lyot stage of a liquid crystal tunable filter (LCTF) system.

The operation of an LCTF may be understood by considering a simplified Lyot filter stack, in which $(N+1)$ polarizers are separated by N layers of liquid crystals sandwiched between birefringent crystals. The optical retardation, R nm, introduced by birefringent crystals is dependent on the thickness of the crystal, d nm, and the difference between the refractive index of the ordinary ray, n_o, and the extraordinary ray, n_e, at the wavelength of interest:

$$R = d(n_e - n_o) \tag{1.7}$$

The velocities of the extraordinary and ordinary ray differ, and these emerge from the stack with a phase delay, Γ radians, that is dependent upon the wavelength, λ, of the radiation:

$$\Gamma = \frac{2\pi R}{\lambda} \tag{1.8}$$

The transmittance of the crystal, T, is given by:

$$T = 0.5\cos^2(\Gamma/2) \tag{1.9}$$

In a typical Lyot filter, crystals are often selected so that transmission has its maximum value at the wavelength determined by the thickest crystal retarder, with

other stages in the filter serving to block the transmission of unwanted wavelengths. The spectral region passed by the LCTF is dependent upon the choice of polarizer, the optical coating and the liquid crystal characteristics (nematic, cholesteric, smectic, etc.) In practice, a Lyot LCTF may have as many as 11 polarizers and 10 liquid crystalline layers, and is sometimes equipped with an internal microprocessor to tune all of the stages.

Wavelength scanning in NIR hyperspectral imaging spectrometers has also been accomplished with both a scanning monochromator and an acousto-optic tunable filter (AOTF.) AOTFs are also frequently used in confocal fluorescence microscopes. AOTFs are electro-optical devices that function as electronically tunable filters and rely on a birefringent crystal, the optical properties of which vary upon interaction of the crystal with an acoustic wave. The resulting compression and rarefaction of the crystal give it the properties of a diffraction grating. Changes in the acoustic frequency alter the grating constant, which enables the wavelength to be tuned very rapidly. The switching time is limited only by the acoustic transit time across the crystal, and is rarely greater than 50 μs. AOTFs designed for operation in the NIR region typically consist of an optically anisotropic tellurium dioxide crystal to which a piezoelectric transducer is bonded. In response to the application of an oscillating radiofrequency electrical signal, the transducer generates a high-frequency acoustic wave that propagates into the crystal. The alternating ultrasonic acoustic wave induces a periodic redistribution of the refractive index through the crystal, which then acts as a transmission diffraction grating. Changing the frequency of the transducer signal applied to the crystal alters the period of the refractive index variation and, therefore, the angle through which the radiation is diffracted, and hence the wavelength band that reaches the detector. The design parameters that affect resolution include the dispersion constant of the crystalline material (related to degree of birefringence), the incidence angle and the acousto-optic interaction length. The relative intensity of the diffracted beam is determined by the amplitude (power) of the signal applied to the crystal and by the widths of the entrance and exit slits of the monochromator.

One of the more important parameters governing which of these wavelength selection devices to use is their bandpass – that is, the full-width at half height (FWHH) of their transmittance window. The typical bandpass of a LCTF is 5 nm. As the FWHH of most bands in the NIR spectrum is greater than 10 nm, a bandpass of 5 nm is more than adequate for NIR hyperspectral imaging. The LCTF has a far higher optical throughput than a monochromator operated at 5 nm resolution (although when the size of the sample being examined is very small, as it is in any microscopic measurement, the potential throughput advantage is rarely met in practice).

The bandpass of a typical AOTF ranges from several nanometers to tens of nanometers for the visible and NIR spectral regions. This resolution is suitable for fluorescence spectroscopy where bands are very broad, and is just adequate for Raman hyperspectral imaging, albeit with lower resolution than may be achieved with a monochromator (see Section 1.5). A NIR spectrometer based on an AOTF has also been sold commercially. However, the transmission of these devices for

NIR hyperspectral imaging is somewhat poorer than that of LCTFs, and they degrade the image quality slightly more than LCTFs. The optical efficiency of monochromators for NIR hyperspectral imaging is poorer than that of both LCTFs and AOTFs. Thus, despite the fact that the FWHH of the pass-band of a monochromator can be made much narrower than that of LCTFs and AOTFs, the highest performance for NIR microspectroscopy is usually found when wavelength selection is accomplished through the use of one of these devices rather than a monochromator.

The NIR hyperspectral imaging spectrometers designed by Malvern Instruments are equipped with a Stirling-engine-cooled indium antimonide (InSb) FPA detector with 320 pixels in one dimension and 256 in the other (total 81 920 pixels) that operates in the range 1200 to 2450 nm. Wavelength tuning is achieved by an LCTF, such that the entire spectral range can be covered in 2 min. Alternatively, as described above, if the signal from just a few wavelengths is all that needs to be measured, the LCTF allows rapid switching between a few selected wavelengths and the measurement is over in a few seconds. A short-wavelength alternative instrument is also available that is equipped with an InGaAs FPA detector that operates in the range from 950 to 1720 nm.

Because this instrument is designed for NIR operation, it is possible to use a microscope with refractive optics. In the case of the Malvern Instruments system, a refractive objective that has 1× magnification is used. With this lens, the sample is imaged directly onto the FPA detector. This objective can be easily removed and objectives with higher (micro mode) or lower (macro mode) magnification installed. The initial alignment of the sample is performed manually, although if a series of samples is to be measured then a programmable sample stage enables the sequential analysis of multiple samples.

It is probably true to say that instruments for NIR hyperspectral imaging are more versatile and rugged than corresponding instruments used to measure mid-IR and Raman spectra. However, they have two disadvantages. The first problem is that the absorptivities of the overtone and combination bands in the NIR spectrum are far weaker than those of corresponding fundamentals from which they are derived. For measurements in the transmission mode, the ideal sample thickness is one that yields a low-noise spectrum with bands that are strong enough to allow rapid identification or quantification. For mid-IR spectrometry, this thickness is about 10 μm. As the center wavelength of mid-IR spectra is about 5 μm, the sample thickness is approximately equal to the smallest dimension in the xy plane that can be observed – that is, the diffraction limit when NA is approximately equal to 0.6. For conventional NIR spectrometry (1200–2450 nm), on the other hand, the absorptivities of the stronger bands are an order of magnitude less than the stronger fundamentals from which they are derived, and so the sample thickness should be at least 100 μm. However, the diffraction limited spatial resolution for NIR measurements is less than 3 μm if optics with a NA-value of 0.6 are used. Thus, even though the ultimate spatial resolution is, in principle, determined by the optics of the spectrometer, in practice this resolution is never achievable because the thickness of the sample means that the diameter of the beam waist

at the top or bottom surface of the sample is larger than the diffraction-limited spatial resolution.

For short-wavelength NIR spectra (950–1720 nm), where the absorption bands are caused by transitions to the third or fourth vibrational states of C–H, N–H and O–H stretching modes, along with weak combination bands, the situation is even worse because bands are so weak that the sample thickness must be increased to about 500 μm, even though the diffraction limit is less than 2 μm. It is at least in part for this reason that NIR hyperspectral imaging is rarely used for measurements with very high spatial resolution. Thus, the standard objective of the Malvern Instruments imaging spectrometer, for example, is a refractive lens with 1× magnification and a low numerical aperture.

The second disadvantage of NIR hyperspectral imaging is more subtle, as it is only evident for measurements of powders. Perhaps the most common application of NIR hyperspectral imaging is in the characterization of intact pharmaceutical tablets by DR spectrometry. These measurements have a significant limitation in terms of their spatial resolution caused by the effect of light scattering. Photon time-of-flight measurements [51–57] have shown that photons in diffuse transmission and reflection measurements emerge from compacted powdered samples (e.g., pharmaceutical tablets) in a time that is much greater than would be expected if no scattering had taken place. In analogous measurements made by mid-IR DR spectrometry, Averett and Griffiths [58] estimated that the average path traveled by mid-infrared photons through very weakly absorbing samples is at least 100 particles, strongly implying that photons do not emerge from the same point at which they enter the sample. The greater the particle size, the more strongly a given particle will absorb at a given wavelength. Similarly, the greater is the scattering coefficient, the fewer particles are encountered by photons in a DR measurement and the better the spatial resolution. For scattering samples, this effect clearly has a highly deleterious effect on spatial resolution. In DR measurements, photons are extensively scattered on entering the sample, passing through several particles (often much more than ten) before re-emerging from the top surface.

The effect of scattering on spatial resolution in DR/NIR imaging has recently been discussed by Hudak *et al.* [59]. These authors measured the DR spectrum of polystyrene powder, but then placed a clear polystyrene window of known thickness over the sample and remeasured the spectrum. From the increase in the intensity of the polystyrene bands, it was possible to show that the effective path-length through the powder was 1 mm (±~50%). Yet, the more intense the band measured, the shorter was the path-length calculated (although the authors did not recognize the fact that the path-length varied inversely with the absorptivity). The group then devised a way to correlate the effective path-length with the sampling volume, by using a random walk model to estimate the volume sampled by a typical photon (which they called a 'voxel'). It was calculated that the average path-length – that is, the sampling radius from which 68% (one standard deviation) of the measured intensity imaged onto a single detector pixel originates – was between 30 and 50 μm. Moreover, it is this distance – which is well over an order of magnitude greater than the diffraction limit – that determines the spatial resolu-

tion of NIR imaging measurements made in DR mode. As the spatial resolution of NIR hyperspectral imaging measurements of scattering samples (e.g., pharmaceutical tablets) is far larger than the diffraction limit, it is clear that NIR DR imaging is best used to characterize samples with a particle size that is far larger than the diffraction limit.

An alternative approach for NIR hyperspectral imaging to that described above is to use a Fourier transform NIR (FT-NIR) spectrometer. As the design of FT-NIR microspectrometers is more similar to that of instruments for mid-IR hyperspectral imaging than the dispersive instruments described above, they will be described later (see Section 1.6).

1.5 Raman Hyperspectral Imaging

Both, Raman mapping and imaging involve the use of CCD array detectors. In mapping, the spectrum of a point of the sample is dispersed across the detector, and the sample is moved when each spectrum has been measured. In Raman imaging, on the other hand, the image of the sample at a single wavelength is focused on the detector and the wavelength is changed after each measurement. Raman imaging methods can be broadly classified as either line imaging or wide-field source illumination approaches [60]. In the line approach, a cylindrical lens or a Powell lens is employed to distribute the laser beam in one direction across the sample. The Powell lens (which is a combination of a cylindrical lens and a prism) may be visualized as a prism with a small radius at one edge, which operates as a cylindrical lens with its radius of curvature decreasing from center to edge. The effect is a monotonic decrease in beam divergence from center to edge, so that the generated line has a near-uniform intensity along its length [61]. The laser line dimension is oriented parallel to the direction of the entrance slit of a polychromator, so that the spectrum is dispersed in the short direction of the CCD. This approach reduces the duration of the experiment by $\sqrt{n}$, where n is the number of image pixels, assuming that the laser power per pixel is kept constant. The spatial resolution parallel to the laser line is the convolution of the microscope magnification by the pixel size, while in the perpendicular direction it is equal to the width of the laser line convolved by the scanning precision of the instrument. As a result, the resolution in one dimension is frequently greater than in the second direction.

In global (wide-field) imaging, the entire sample field-of-view is illuminated by defocusing the laser. The scattered radiation is usually first passed through a notch filter or a long-pass filter to remove the Rayleigh-scattered radiation, and then through a device that blocks all but one wavelength region. This device may be a monochromator, a dichroic filter, an acousto-optic tunable filter or a liquid crystal tunable filter, with the latter being generally favored. The wide-field approach is generally favored over line-scan imaging when high-fidelity images at a limited number of wavenumbers are desired. In wide-field imaging, the spatial resolution

is determined by the convolution of diffraction, the CCD pixel size and the microscope magnification at the focal plane of the CCD.

Surprisingly, global laser illumination leads to sample heating degradation at much lower laser intensities than point illumination, because of the inefficiency in conducting heat away from a surface sheet rather than a point. For steady-state measurements at a given total laser power (in W), the optical damage threshold for a given material scales as the square root of the illuminated area (rather than linearly with the area). Thus, the laser intensity (in W m^{-2}) required to damage a sample is higher for a point illumination than for line illumination, which is in turn higher than for area illumination. There is still an advantage to distributing power over a wider area; it is just that this so-called 'power distribution advantage' is not as great as was previously assumed [62].

As noted in Section 1.3, confocal microscope designs have been used in several Raman microspectrometers that allow sample mapping by moving the sample between the measurement of each spectrum. However, confocal microscopy cannot be used for wide-field Raman imaging as the entire region of the sample of interest must be illuminated, and clearly the 'light source pinhole' (see Figure 1.12) in confocal microscopes does not allow this. For hyperspectral Raman imaging, the high image quality attained by the use of confocal optics and mapping is sacrificed somewhat for data acquisition speed. However, this approach is only fast if an image is to be acquired at a single wavelength; for the acquisition of full spectra, it can be very slow.

One of the first Raman imaging spectrometers to be produced in the USA was designed and fabricated by Levin's group at the U.S. National Institutes of Health (NIH) [63]. The wavelengths for this instrument were controlled by a TeO_2 AOTF. The instrument produced high-fidelity, large-format images with a theoretical spatial resolution of about 1 μm, although because of dispersion by the TeO_2 crystal the finite spectral bandwidth of the AOTF resulted in a slight smearing of the output image along one axis. This degradation, which is given by the internal beam spread in the crystal, $\Delta\theta_{di}$, could be estimated from the approximate relationship reported by Suhre *et al.* [64]:

$$\frac{\Delta\theta_{di}}{\Delta\lambda} = \left(\frac{\Delta n}{n_0\lambda_0}\right)(\sin 4\theta_1 + \sin 2\theta_1)^{1/2} \tag{1.10}$$

where $\Delta\lambda$ is the passband (2 nm), λ_0 is the center wavelength (700 nm), Δn is the difference in refractive index of TeO_2 for the ordinary and extraordinary rays at λ_0 (0.138), n_0 is the refractive index of TeO_2 for the ordinary ray (2.177), and θ_1 is the angle between the incident beam and the optical axis of the crystal (22.5 °); the values for the AOTF used by Goldstein *et al.* are given in parentheses. These values give an external beam spread, $\Delta\theta_{di}$, of 0.13 mrad (0.0037 °); this value may be compared with the diffracted beam spread of 0.19 mrad caused by the 7 mm^2 aperture presented to the AOTF entrance pupil. In total, these values would lead one to predict that the image resolution along one axis would be degraded by about a factor of 2.5 on passage through the AOTF. For each AOTF passband frequency,

the image on the CCD will be shifted slightly because of dispersion by the crystal, and software correction is needed if the visual and Raman images are to be correlated.

In the instrument described by Goldstein *et al.* [63], the 647.1 nm beam from a krypton ion laser was delivered to the sample by an infinity-corrected microscope objective using an epi-illumination scheme. For this, light from the rear housing was passed down a horizontal shaft and then reflected down through the objective to the sample. The 180° back-scattered light was returned to the objective and then to the spectrometer. Wavelength selection was accomplished by an AOTF that could provide either random or continuous wavelength selection. The epi-illumination scheme was seen to preserve the linear polarization of the incident laser beam. Because the AOTF is polarization-sensitive, a half-wave plate was used to rotate the plane of polarization by 180° in order to preserve the AOTF output. The collimated output from the AOTF was first imaged by a tube lens, and then by a projection lens onto a liquid-nitrogen-cooled silicon CCD array. One, or occasionally two, holographic notch filters were placed in front of the detector to eliminate stray radiation from the Rayleigh line. These filters transmitted between 75 and 80% of the Raman emission beyond 75 cm^{-1} of the Rayleigh line.

In order to minimize the data acquisition time, the overall magnification of this system was made as small as possible, consistent with the spatial resolution desired. As the image is sampled by the discrete pixels of the CCD camera, the Nyquist sampling criterion must be obeyed to avoid the generation of artifacts. There is an explicit relationship describing how the number of counts per pixel depends on the optical design. It is known from Equation 1.3 that the radius of the Airy disk r is equal to $0.61\lambda/NA$. If the size of the CCD pixel is p, then the Nyquist sampling criterion requires that the overall magnification, M, satisfies the condition that $Mr > 2p$. Goldstein *et al.* designed their system such that $Mr = 2.3p$; in other words, the smallest resolvable feature was sampled by at least two pixels [63]. It should be noted that this rule of thumb is equally applicable to imaging spectrometers, where the spatial resolution of the measurement should be spread over at least two pixels.

The instrument reported by Goldstein *et al.* is shown diagrammatically in Figure 1.22. Also shown (in Figure 1.23a) is the Raman image of 1 μm-diameter polystyrene beads, obtained by recording the signal at 1000 cm^{-1} from one of the pixels. Figure 1.23b shows the spectrum measured from one of the pixels in the region of this band. Note that its FWHH band is at least 25 cm^{-1}, whereas the true FWHH of this band is less than 10 cm^{-1}, thereby demonstrating the trade-off between magnification, image quality, spectral resolution and data acquisition time in Raman mapping. A similar system explicitly designed for *in vivo* tissue diagnostics has been described by Vo-Dinh *et al.* [65].

ChemIcon, Corp. (now ChemImage, Corp.) market a Raman imaging spectrometer that shares some of the features of the NIH instrument reported by Goldstein *et al.* but, nonetheless, has some significant differences. First and foremost, wavelength selection is accomplished through the use of an LCTF rather than an AOTF. The spectral bandpass of this instrument is 9 cm^{-1}, and it has the capability of

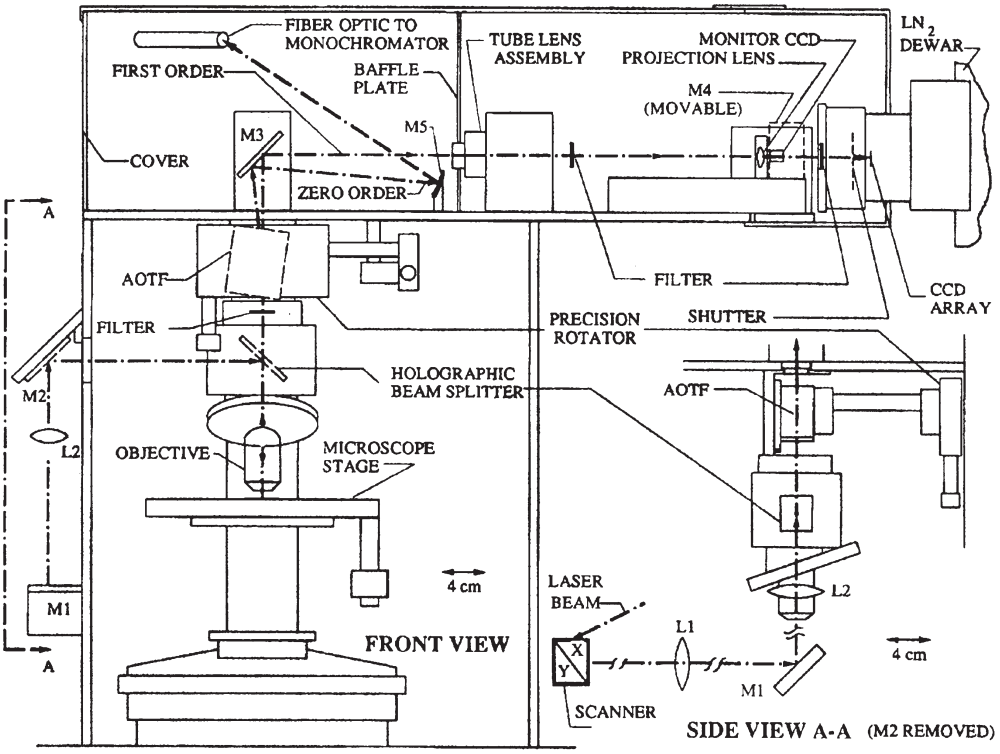

Figure 1.22 Schematic diagram of the Raman imaging microscope reported by Goldstein *et al.*. Reproduced with permission from Ref. [63].

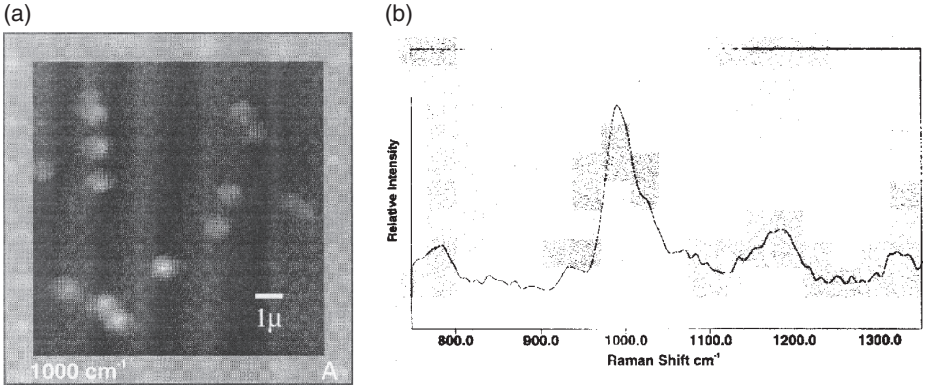

Figure 1.23 (a) Image of 1 μm-diameter polystyrene spheres acquired using the instrument shown in Figure 1.21 by holding the AOTF at 1000 cm^{-1}; (b) Spectrum from one pixel of the CCD. Reproduced with permission from Ref. [63].

being tuned at finer increments. It is also claimed that a spectral resolving power of better than 0.1 cm^{-1} has been consistently achieved, although this term probably refers to the accuracy to which the center wavenumber of the LCTF bandpass may be set, as the FWHH of the passband of an LCTF is never as small as 0.1 cm^{-1}. The Raman microscope sold by Renishaw, Inc. may also be used in the imaging mode, by holding the monochromator at a certain wavelength for each time increment. However, the Renishaw instruments are mainly used in the Raman microscopy and mapping modes.

1.6 Mid-Infrared Hyperspectral Imaging

1.6.1 Spectrometers Based on Two-Dimensional Array Detectors

The first true chemical imaging microspectrometer was reported by Levin's group at NIH and Marcott's group at Procter and Gamble [66], who used a Bio-Rad (now Varian[2)]) FTS 6000 step-scan FT-IR spectrometer equipped with a UMA-500 microscope. In their earliest instrument, the single-element detector mounted in the microscope was replaced by an indium antimonide (InSb) FPA detector with 64×64 elements imaging an average spatial area of $500 \times 500\,\mu m$. A CaF_2 lens was used to focus the sample area onto the FPA detector. As InSb has a cut-off of 1800 cm^{-1}, the fingerprint region of the mid-IR spectrum could not be measured with this instrument.

A short time later, Levin's group modified step-scan FT-IR spectrometer to operate with a mid-IR MCT FPA detector. Unlike most MCT detectors used in FT-IR spectrometers, which operate in the photoconductive (PC) mode, the pixels of MCT FPA detectors operate in the photovoltaic (PV) mode. As noted in Section 1.2.2, the cut-off wavenumber of narrow-band PC MCT detectors is about 750 cm^{-1}. The PV detector elements used in MCT FPA detectors have the same high sensitivity as narrow-band PC MCT detectors, but the cut-off wavenumber is higher, at about 850 cm^{-1}.

The first commercial instrument employing the concepts developed by Levin's group was designed by Bio-Rad and marketed as the *Stingray* in 1995. This instrument is shown schematically in Figure 1.24. In order to maintain the image

2) Like several other corporations in the field, the company now doing business as Varian has undergone several name changes. It was first known as Digilab, Inc. Founded in 1969, Digilab developed the first FT-IR spectrometer of the modern era, that is the first with He–Ne laser referencing, the use of a pyroelectric (TGS) detector and the first under minicomputer control. Digilab was purchased by Bio-Rad in 1978. In 2001, Bio-Rad sold the company to a group of private investors, who renamed the company Digilab LLC. The group sold Digilab to Varian in 2004. During each of these manifestations, this organization made many of the innovations that have led to the remarkable popularity of FT-IR spectroscopy today. In this chapter, the name of the company will be given as it was when the work was reported.

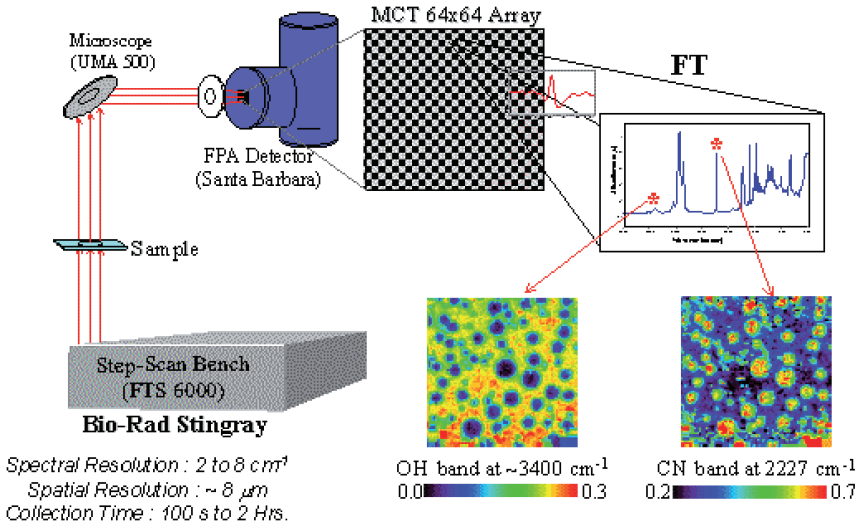

Figure 1.24 Schematic diagram of the Bio-Rad Stingray hyperspectral imaging spectrometer. Illustration courtesy of Varian Corporation.

quality, a ZnSe lens was used to focus the sample image onto a MCT FPA detector, rather than the Cassegrain system used in most microscopes. The instrument is equipped with a germanium long-pass filter to block visible and short-wave NIR radiation, and hence to prevent detector pixel saturation and improve the SNR. A lightly sanded KRS-5 plate placed in the beam path before the condenser further improves the spatial homogeneity in the camera field-of-view, and also prevents the detector elements in the center of the array from saturating.

These first attempts during the mid 1990s at true mid-IR FPA imaging using a 2-D MCT FPA detector were based on the detectors mounted in military heat-seeking missiles, and the spectrometers that resulted are now termed 'first-generation' instruments. As the detectors used in such instruments were not designed specifically for spectroscopic imaging, they had a number of limitations, one being a tendency for pixels to 'delaminate' and separate from the substrate. As these first-generation detectors were designed essentially for 'one use' applications, they were unable to cope with the thermal stresses of repeated heating–cooling cycles associated with liquid nitrogen cooling.

Another major limitation arose from the need to employ a step-scan interferometer. This necessity arose from the relatively slow read-out rates of these first-generation FPAs, which were of the order of only a few hundred Hertz. The read-out rate (or *frame rate*) of a FPA detector determines the type of interferometer that must be used for FT-IR imaging, as the FPA cannot be triggered (for data transfer) any faster than its maximum read-out (frame rate) speed. As the first-generation FPAs were only capable of frame rates in the hundreds of Hz, and rapid-scanning interferometers required a faster frame rate, the use of step-scan

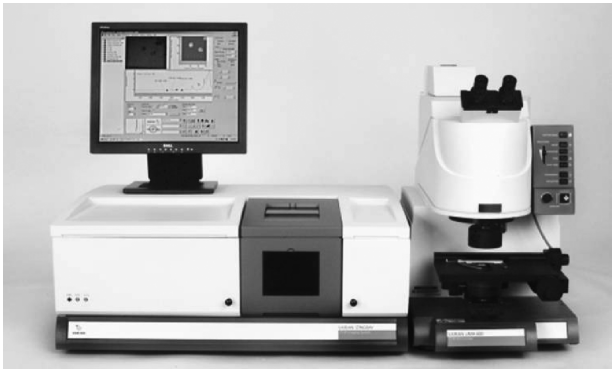

Figure 1.25 The first commercial rapid-scanning FPA chemical imaging system, introduced in 2001 by Digilab (now Varian Corporation).

interferometers – where the movable mirror of the interferometer could be held a given optical path difference for several seconds – was mandated.

In 1999, Snively *et al.* described the first report of the use of a rapid-scan interferometer in conjunction with a small first-generation focal-plane array for spectroscopic imaging [67]. In an attempt to design a mid-IR chemical imaging system designed specifically for spectroscopic applications, Digilab, together with the FPA supplier, developed and marketed the first commercial mid-IR 'rapid-scan' imaging systems in 2001, with the launch of the 'second-generation' FPA, designed specifically for spectroscopic chemical imaging (see Figure 1.25). These second-generation FPAs had frame rates which were an order of magnitude faster than their first-generation counterparts, such that the standard laboratory-type rapid-scanning FT-IR spectrometer could now be used for chemical imaging, with a significantly increased affordability yet reduced complexity. This, in turn, led to an increased use and application of mid-IR imaging spectrometers.

In addition to pioneering the developments in FPA detectors designed specifically for fast mid-IR hyperspectral imaging, Digilab redesigned their microscope to launch the first instrument designed specifically to cater for the unique requirements of FPA-based imaging. Such improvements included a wider and more uniform illumination field of view (FOV) of up to $700 \times 700\,\mu m$, removing the need for any diffusers, the removal of refractive focusing optics and the introduction of optical zoom capabilities for changing the pixel size at the sample plane from 5.5 to 11 μm (with a corresponding increase in FOV). Despite the availability of 'rapid-scan' FPA mid-IR chemical imaging systems since 2001, it often still thought that mid-IR hyperspectral imaging spectrometers require step scanning, this being a legacy from the original first-generation, military-based FPAs of the mid 1990s.

Generally speaking, the larger the array, the slower the read-out frame rates of the FPA. The frame rates of today's second-generation FPAs range from several kHz for the smaller 16×16 and 32×32 FPAs, to just over 1 kHz for the largest

commercially available (128 × 128) FPAs. The ability to operate these FPAs at rapid scan speeds depends on the frequency at which the spectrometer triggers the FPA. The sampling of signals from FPAs is similar to that for a standard detector such as DTGS, whereby the detector response is recorded as a function of opd to provide an interferogram. For FPAs operated in PV mode, the FPA response (for each pixel) is triggered by the interferometer. At each trigger, the pixel response is read out in 'snapshot' mode, whereby all pixels are read out simultaneously, processed and transferred to the data system to provide for an interferogram datum point for each pixel in the FPA at each opd. The triggering rate must, of course, be less than the maximum frame rate of the FPA; for a 64 × 64 FPA, the maximum frame rate is 3.77 kHz. Because of the discrete speed settings available on most commercial FT-IR spectrometers, for a spectral range of 7900 cm^{-1} (the Nyquist wavenumber for a He–Ne laser-referenced system with an undersampling ratio of 2), the fastest scan speed that can currently be used to collect data from a 64 × 64 FPA is 2.5 kHz. The use of an undersampling ratio of 2 allows for the data to be collected without any aliasing into the mid-IR spectral region (<4000 cm^{-1}).

The data collection (interferometer) speed can be increased up to 5 kHz, by further undersampling the interferogram. An undersampling ratio of 4 (whereby the FPA is triggered for data read-out at every fourth He–Ne laser zero crossing; that is, every second wavelength of the HeNe interferogram) provides for a Nyquist wavenumber of 3950 cm^{-1}. However, in order to prevent spectral artifacts caused by aliasing from appearing in the spectrum, a low-pass filter must be mounted in the optical path to prevent radiation with wavenumbers above 3950 cm^{-1} from reaching the FPA detector. The insertion of such a filter has the added benefit of limiting detector saturation by preventing light from outside the spectral region of interest from reaching the detector, hence allowing longer integration times to be utilized for an increased SNR. The increase in interferometer scan speed to 5 kHz still means that the FPA is being triggered at 2.5 kHz, as now the triggering at every fourth zero crossing instead of every second zero crossing means that the interferometer scan speed can be increased twofold to 5 kHz. As the FPA is in fact still being triggered at 2.5 kHz, the actual frame period is hence the reciprocal of the frame rate at 0.40 ms. With typical integration times of 0.01 to 0.05 ms for high-throughput systems, it is clear that the FPA is typically integrating for only a fraction of the fully available frame period. This is a result of the high sensitivity of the MCT material requiring only a short integration time. Despite such advances in FPA design – and in particular of the electronics – the frame rates are still relatively slow. An ideal design would have the maximum probable integration time matched to the frame period. For example, assuming that a maximum integration period of 0.05 ms is required and the frame period is designed to match, this would result in a frame rate of 20 kHz. Although no commercially available FPA has such high frame rates, the technological advances observed in modern electronics indicates that these will be achievable in the foreseeable future.

For imaging measurements using a step-scan FT-IR spectrometer, the interferometer mirror is held at a constant position (usually at the zero-crossing of the laser interferogram) while the signal from each pixel is recorded by the ADC. This

process may be repeated several times at the same sampling position to allow *frame co-addition*, whereby the signals from all pixels are averaged several times before the interferometer mirror is stepped to the next sampling position. In practice, although frame co-addition works well until about 20 frames have been averaged, further averaging does not lead to any great improvement in the SNR. When the signal from each pixel has been averaged the required number of times, the interferometer mirror is stepped forward to the next sampling position, and this process is continued until sufficient data points have been measured to achieve the desired spectral resolution. Snively and Koenig showed that N successive images could also be signal averaged for the expected improvement in SNR of $\sqrt{N}$ [68]. When all the data have been acquired, the interferograms are converted to single-beam spectra, ratioed against the corresponding single-beam background spectrum, and converted to absorbance.

By analogy with Equation 1.2, Sniveley and Koenig showed that the SNR on the baseline of spectra measured with an imaging FT-IR spectrometer is given by:

$$\mathrm{SNR} = \frac{0.12\pi A\left\{1-\sqrt{1-(NA)^2}\right\}U_{\tilde{\nu}}(T)\Delta\tilde{\nu}D^*\sqrt{t}}{A_D^{1/2}} \tag{1.11}$$

where NA is the numerical aperture and A is the area of the sample imaged onto the pixel. All the other parameters have the same meaning as in Equation 1.2 [68]. The factor of 0.12 is analogous to the efficiency term ξ in Equation 1.2. Sniveley and Koenig used this equation to compare the performance of FT-IR imaging and single-detector microspectrometers and found that, for measurements near the diffraction limit, the performance of imaging spectrometers should be higher than that of standard FT-IR microspectrometers if it is assumed that the D^* of the detectors and the area of the sample imaged onto the pixel are the same in both types of instruments. (In practice, the D^* of PV-MCT detectors is slightly higher than that of PC detectors for signals modulated at frequencies greater than 1 kHz, although the difference is small.) The biggest advantage of the imaging spectrometers is in the A_D term for array detectors. Whereas, most FT-IR microscopes are equipped with 250 µm detectors, the pixel size in most FPAs is 40 µm, which leads to an advantage in $\sqrt{A_D}$ by a factor of ~2.5 for the imaging spectrometer for measurements made close to the diffraction limit of spatial resolution.

However, the benefit in SNR of an imaging system over a single point system when close to the diffraction limit is much greater than a factor of 2.5. The probable reason for the significantly greater performance of the imaging spectrometers is that Equation 1.11 fails to account for the sample aperture (and its resulting degradation in étendue) when a spectrometer is operated close to the diffraction limit. Because they do not require an aperture, each entire pixel is fully illuminated in imaging systems. Consider the case of a measurement made at close to a diffraction limit of, say, ~10 µm (therefore with a 10 µm aperture). For a spectrometer with a single-element 250 µm detector, only 0.16% of the detector surface is illuminated, with the remaining 99.84% contributing only noise. When this factor is taken into account, together with the 2.5-fold improvement predicted by Equation

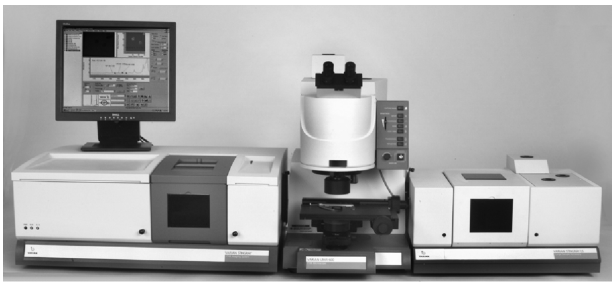

Figure 1.26 The 'Large Sampling Accessory' by Varian, provides for FPA chemical imaging at a 1:1 magnification for the analysis of 'macro' samples. Illustration courtesy of Varian Corporation.

1.11, imaging spectrometry recorded close to the diffraction limit provides for SNR benefits of many orders of magnitude!

Although chemical imaging is typically performed with a microscope, it need not be limited to microscopes and samples in the micro domain. In 1998, Digilab released the 'Large Sampling' (LS) accessory; this consisted of an external sample compartment unit in which the FPA detector could be mounted and transferred as required between the microscope and the LS (see Figure 1.26). The LS accessory is mounted either directly off the FT-IR spectrometer or off the microscope via 'pass-through' optics that allow the IR beam to bypass the internal optics of the microscope. Under this configuration, the overall magnification is 1:1, so that the pixel size at the sample plane now matches that of the native FPA pixel size at $40 \times 40\,\mu m$. Therefore, with a 128×128 FPA, sample areas of up to 5.1×5.1 mm can be imaged at once.

1.6.2
Spectrometers Based on Hybrid Linear Array Detectors

An alternative approach to hyperspectral imaging, namely a hybrid of imaging and mapping, was reported in 2001 by PerkinElmer (PE) as the *Spectrum Spotlight*. This instrument is an imaging FT-IR spectrometer that incorporates a linear array of 16 photoconductive narrow-band MCT detectors interfaced to a relatively inexpensive rapid-scanning interferometer. Although this detector is commonly (and perhaps for the sake of simplicity) often referred to as a 1×16 linear array detector, the pixels are in fact arranged in a 2×8 format. As the cut-off for the narrow-band PC-MCT detectors used in this spectrometer is about $720\,cm^{-1}$, the spectral range of the instrument is at least $130\,cm^{-1}$ wider than that of the PV MCT FPA detectors incorporated into most other hyperspectral imaging FT-IR spectrometers. The signals from each of the 16 detectors in the linear array are digitized simultaneously with separate ADCs. The sample is mounted on a computer-controlled stage that can be rapidly repositioned to allow the spectra from an adjacent region to be

measured once the spectral data from a given stage position have been acquired. The spectra are then quilted together to produce the image. This process is repeated until the entire spatial region of interest has been covered. In addition to this linear detector array, a single 100 µm medium-band MCT detector is mounted in the same Dewar flask, that allows individual spectra to be acquired over a wider range than the spectra measured with the array. A similar instrument is now available from Thermo Fisher Corporation that consists of a 28-pixel linear array arranged in a 2×14 pixel format.

Much confusion exists as to the advantages and disadvantages of linear-array versus FPA-based imaging systems, and detailed analysis and comparison is beyond the scope of this chapter. However, Bhargava *et al.* proposed a useful metric to aid in comparing the performance of two imaging systems that can be conveniently applied to the comparison of these two systems [69]. The figure of merit defined is the pixels per minute 'pixpm', and compares the performance of two imaging systems relative to each other for a specified SNR at defined spectral and spatial resolutions. The ratio of the pixpm values of two instruments is given by:

$$R_{21} = \frac{n_2}{n_1}\left(\frac{t_1}{t_2}\right)\left(\frac{SNR_2}{SNR_1}\right)^2 \tag{1.12}$$

where R_{21} is the ratio of the pixpm of system 2 to system 1, n_i is the number of pixels collected over the defined sample measurement area, t_i is the time required to collect the image (of either 1 scan or to achieve the required SNR) and SNR_i is the average SNR achieved over the sample measurement area. Hence, the relative performance is linearly related to the time and number of pixels collected and to the square of the SNR.

Let us assume the sample area to be measured is moderate in size (say, 700×700 µm), and is to be collected at high spatial resolution and 4 cm^{-1} spectral resolution at a SNR of 200. Based on the manufacturers' typical specifications, if all other parameters are kept equal, we have:

	System 2 ($i = 2$)	**System 1 ($i = 1$)**
	64×64 FPA (5.5 µm projected pixel size)	16-element linear array (6.25 µm projected pixel size)
n_i (number for a pixels collected for a 700×700 µm sample area)	16 384 (four tiles)	12 544 (784 line scans)
t_i	5 min (32 scans co-added)	150 min (16 scans co-added)
SNR	200	200

Based on the above comparison, the FPA imaging system is 39-fold better, under the specified conditions, despite requiring twice as many scans (32 versus 16). This result can be rationalized by considering the massive multichannel advantage of a 64×64 FPA (4096 detectors) over a 16-element linear array. For example, the FPA has 256 times as many detectors collecting data simultaneously compared to the linear array. To cover the same $700 \times 700\,\mu m$ area, the 64×64 FPA, with its $5.5\,\mu m$ pixel size requires a four-tile mosaic, whereas the 16-element linear array in its high spatial resolution mode of $6.25\,\mu m$, requires 784 separate line scans. Thus, even though the time during which a given interferogram can be acquired with the linear array is shorter than when an FPA is used, the FPA-based spectrometer required a total of 128 (4×32) scans while the instrument that incorporated the linear array required 12 544 (16×784) scans. Thus, the acquisition of almost 100-fold more scans results in a significantly slower overall time of collection when the linear array is used. The smaller pixel size of the FPA system ($5.5\,\mu m$) compared to the linear array ($6.25\,\mu m$) results in more pixels being collected for the same sample measurement area which, according to Equation 1.12, further increases the advantage of the FPA-based instrument.

Although the differences between FPAs and linear arrays are not always of this magnitude, they are usually in favor of the FPA-based imaging system. In fact, when employing even larger FPAs, such as the 128×128 FPA, the differences are even larger. Linear array systems are, however, generally at their most efficient when operated at relatively low spatial and spectral resolutions (e.g., $25\,\mu m$ and $16\,cm^{-1}$, respectively) and with only a few co-added scans, where the synchronization of interferometer step and stage travel is most accurately achieved.

1.6.3 Sampling

Imaging can be accomplished by using any of the approaches used in mid-IR mapping, namely transmission, external reflection and attenuated total reflection. In some instruments, the microscope objective can be changed to permit operation at either high or low magnification. The key to any imaging measurement is that the sample should be accurately located at a beam focus so that it can be exactly re-imaged on the array detector. The first applications of mid-IR imaging were performed in the transmission mode, with a few examples of reflection spectroscopy. Imaging by ATR took longer to be reported, even though ATR imaging is by no means a new concept. For example, in his 1967 book *Internal Reflection Spectroscopy*, Harrick showed the visible ATR image of a fingerprint recorded photographically [70].

Despite Digilab (now Varian) having been granted a patent on ATR imaging in 2000 [71], this does not seem to have stopped others from employing this technique, using spectrometers from other manufacturers. Sommer *et al.* [72] used an ATR accessory with a germanium IRE mounted in the external beam of a Stingray spectrometer/microscope. By using the edge profile test (as discussed in Section 1.2.6), the group demonstrated a spatial resolution of about $8\,\mu m$ in the fingerprint

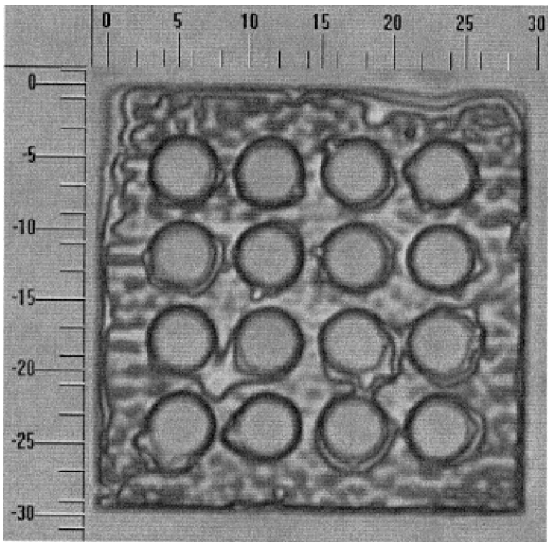

Figure 1.27 Visible image of the patterned PMMA film on a silicon wafer, captured with a 100× objective. The scales on the image are in micrometers. Reproduced with permission from Ref. [73].

region, and claimed also to have shown that the 4× magnification factor associated with the germanium internal reflection element was realized. However, a 4× reduction of the diffraction limit for a microscope with a *NA* of 0.6 should have meant that the spatial resolution was improved to 2.5 μm, and this was not explicitly demonstrated. More recently, Chan and Kazarian reported a detailed study of ATR imaging using a patterned film of PMMA on a silicon substrate [73]; the visible image showed circles of the polymer that were 4 μm in diameter with a separation of 2 μm (see Figure 1.27). Micro-ATR imaging with a germanium IRE ($n = 2.4$) showed that the PMMA circles were resolved when the spectrum was integrated between 1753 and 1672 cm^{-1} (average wavelength, $\lambda_{ave} = 5.8\,\mu m$), but the image tended to wash out at longer wavelengths as the diffraction limit was approached (see Figure 1.28).

Perhaps the most detailed investigation into the resolution of ATR imaging instruments was presented by Everall, who first calculated the edge profile by convolving the image at 1600 cm^{-1} of the interface between the two polymers with the Airy disk, taking into account the 10 μm size of the pixels in the FPA MCT detector [74]. Everall then measured absorbance at 1600 cm^{-1} in each spectrum in the hyperspectral ATR image of a laminate of an acrylonitrile-butadiene-styrene (ABS) polymer in the region of the interface, using a Stingray imaging spectrometer equipped with a diamond ATR element. The fit was remarkably accurate, as shown in Figure 1.29.

Everall also demonstrated the problems of quantitative ATR imaging when trying to measure the image of a sample containing hard spheres with a diameter

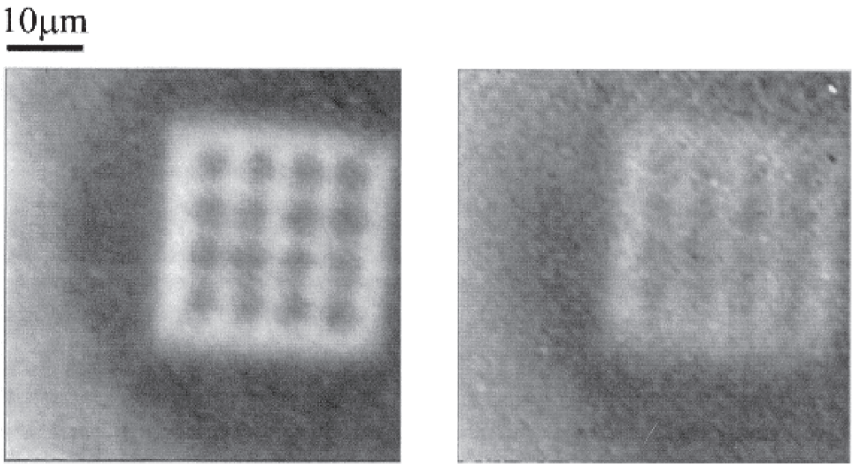

Figure 1.28 Micro-ATR images of the PMMA film on a silicon wafer shown in Figure 1.24 obtained by integrating between (a) 1753 and 1672 cm^{-1} (λ_{ave} = 5.8 μm) and (b) 1179 and 1090 cm^{-1} (λ_{ave} = 8.8 μm). Reproduced with permission from Ref. [73].

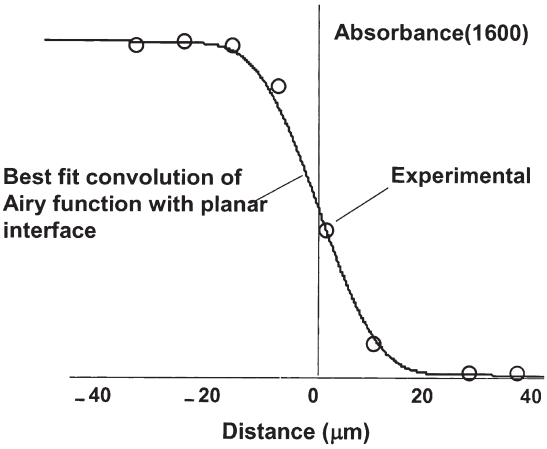

Figure 1.29 Calculated and experimental variation of the 1600 cm^{-1} band of polyurethane as a function of distance from the interface of a polyurethane-ABS laminate. Illustration courtesy of Dr Neil Everall, Measurement Science Group, Intertek Corporation.

equal to or smaller than the depth of penetration. It was shown that a shallow penetration, combined with the finite spatial resolution of an imaging spectrometer, renders ATR insensitive to hard spherical particles with domain sizes ranging between 10 and 150 μm. For large spheres, the shallow penetration depth underestimates the diameter whereas, for small spheres the finite spatial resolution overestimates the diameter due to blurring, causing the apparent size insensitivity of the technique for spheres. Everall's conclusions were equally valid for other irregular inclusions, while flat or 'platey' domains should yield more accurate results. Everall further showed that the compression of soft particles increased their apparent size, albeit in a noncontrolled fashion, and stressed that ATR imaging is nonetheless a valuable technique for assessing variations in the surface composition of polymer samples. It was suggested that, by sectioning the samples, a more accurate picture of the near-surface composition could be obtained.

Everall also measured the images of polystyrene spheres of several diameters using a 1450 cm^{-1} (6.9 μm) band of polystyrene [74], and showed that transmission spectroscopy gave far better estimates of sphere diameter than did ATR imaging. The error in estimating the sphere diameter was approximately 10% when the diameter was ≥50 μm, whereas with ATR imaging the estimated particle diameter was considerably less than the actual diameter. However, when the sphere diameter was ≤10 μm, their apparent diameter as measured by transmission imaging was approximately equal to the diffraction limit (20 μm).

Image-preserving ATR accessories can be mounted in the Varian LS accessory for 'Macro ATR Imaging'. In 2007, Specac – in partnership with and exclusive to Varian (under Varian's 'ATR imaging' patent [71] – released an imaging-specific version of their well-known 'Golden Gate' single-reflection diamond ATR that differed from the standard version by its patented 'image-preserving' optical design [75]. This is necessary if the spatial relationships of the image are to be preserved whilst being propagated through the IRE. The FOV with this accessory may be as large as 640 × 640 μm when used with a 64 × 64 FPA.

Another image-preserving ATR accessory that has been used in conjunction with 'macro imaging' is the Harrick FastIR, which consists of a simple inverted ZnSe prism such as that shown in Figure 1.9a. As the IRE is fabricated from ZnSe rather than diamond, this accessory is less robust, but does offer the advantage of having a considerably larger FOV of up to ~10 × 6 mm when used with a 128 × 128 FPA. These accessories open up a whole new avenue of research, as now one can combine the already proven and well-established benefits of ATR accessories such as limited or no sample preparation with the information-rich content afforded by FPA chemical imaging.

In another Digilab patent [76], a 'side port' adaptor directs the beam that would otherwise enter the objective (in reflection mode), via a 45° flat mirror toward the front of the instrument into an objective now facing outwards. In such a configuration, the sample size is no longer limited by the working distance of the objective (typically ~24 mm). Thus, large samples may be placed in front of the outward-facing objective for measurement (see Figure 1.30). In such a configuration, only the external reflection or ATR modes of sampling are possible. This mode of

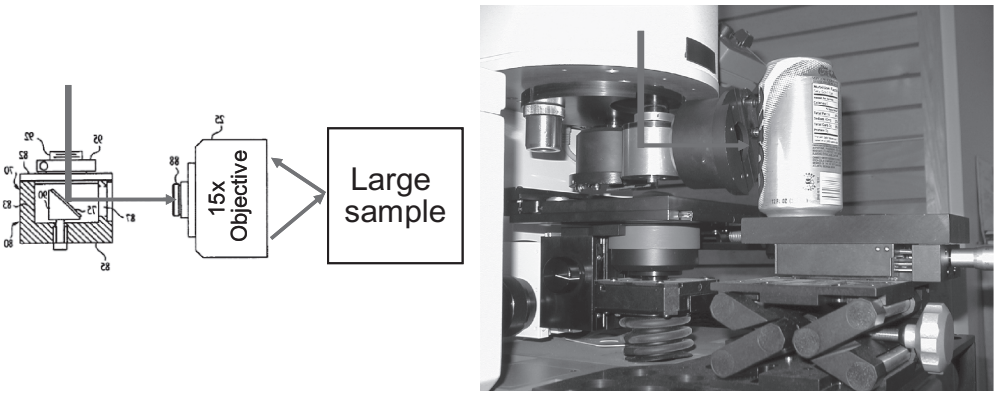

Figure 1.30 Varian's patented side-port adaptor and objective, allowing for the measurement of samples that are too large to be accommodated under the objective's standard 24-mm working distance. Illustration courtesy of Varian Corporation.

measurement makes it conceivably possible for large objects such as complete vehicle bumper bars to be stood on the floor and held in contact with the micro ATR accessory on the outward-facing side port objective.

In summary, ATR imaging has a number of advantages over transmission or external reflection imaging for studying surfaces that do not have spherical or irregular inclusions, not the least of which is the absence of artifacts caused by Mie scattering. Sample preparation is much easier and the diffraction-limited spatial resolution that can be obtained is less than can be obtained by transmission imaging, by a factor equal to the refractive index of the IRE. However, because the depth of penetration is low, the peak absorbance of even quite strong bands can be rather weak, especially if a germanium or silicon IRE is used. Finally, as noted above, if the sample contains spherical or irregular particles, they may not be adequately interrogated by the evanescent wave, making them appear smaller than they actually are. In an interesting example of 'what goes around, comes around', Kazarian's group recently published hyperspectral imaging data of human fingerprints in which trace quantities of drugs of abuse could be detected in a few of the spectra [77]. The science of imaging has certainly come a long way since Harrick's original ATR photograph of a fingerprint.

1.7
Mapping with Pulsed Terahertz Radiation

Vibrational spectroscopy covers the spectral region from about 0.75 μm (~13 500 cm^{-1}) to 1000 μm (10 cm^{-1}). To this point, we have covered the NIR (0.75 to 2.5 μm or ~13 500 to 4000 cm^{-1}) and mid-IR (2.5 to 25 μm or 4000 to 400 cm^{-1}) regions. The final region that will be discussed in this chapter is the far-IR (25 to

1000 μm or 400 to 10 cm^{-1}). Many different types of transition are seen in the far-IR region of the spectrum; these include intramolecular stretching modes involving heavy atoms, skeletal bending modes involving the entire molecules, torsional modes, ring puckering vibrations of small-ring molecules, intermolecular vibrations of hydrogen-bonded molecules and charge-transfer complexes and lattice bands (or phonon modes) [78]. Until only a few years ago, far-IR spectra were difficult to measure and rarely used for chemical analysis. This state of affairs was a result of the fact that the radiative energy emitted by sources of continuous far-IR radiation, such as a Globar or high-pressure mercury lamp, is far lower than the corresponding energy emitted by mid-IR sources. The measurement of far-IR spectra using such sources is slow, even with a FT spectrometer.

In about 2003, a completely new way of generating far-IR radiation was developed such that far-IR spectra could be measured faster and at a higher sensitivity than before [79, 80]. As a result, there has been a renewed interest in this spectral region. In order to distinguish the 'old way' of measuring far-IR spectra from this 'new way', the new technology has been termed terahertz spectroscopy, since the wavenumber region from 1.2 to 130 cm^{-1} corresponds to the frequency region from 0.05 to 4 THz (1 THz = 1×10^{12} Hz).

The source for terahertz spectroscopy is an ultra-short-pulsed laser (usually Ti:Sapphire) that emits a stream of pulses of NIR radiation at ~80 MHz, with each pulse lasting for about 70 fs. The laser pulses are focused on a photoconductive switch (sometimes known as an 'Auston switch') which is a small semiconductor crystal (often GaAs) on which two planar metal electrodes support a large electric field across its surface [81]. The design of these metal electrodes is that of an antenna. The pulses of NIR radiation cause electron-hole pairs to be generated at the surface of the semiconductor, thereby changing the conductance and effectively closing the switch. With a carefully designed antenna, the electron-hole pairs are accelerated by a DC electric field applied across the device, leading to a rapid change in the current density. The changing dipole produces a THz transient in the antenna that is radiated into free space; the resultant effect is the emission of short bursts of broadband coherent terahertz radiation with each laser pulse. The long-wavelength radiation that is generated by this technique can then be collected using a silicon lens.

A small fraction of the NIR laser pulse is also used in the detection process. This radiation is focused onto a second semiconductor device where, once again, electron-hole pairs are generated at the surface. On this device, however, the electric field that is created by the coincident pulses of terahertz radiation induces a measurable photocurrent. The femtosecond laser pulse effectively acts as an optical gate, which is only open for the lifetime of the electron-hole pairs in the semiconductor (<200 fs.) By sweeping the time delay between the arrival of the femtosecond laser pulse and the terahertz pulse, a waveform comprising the terahertz signal as a function of time can be constructed (see Figure 1.31). The Fourier transform of this signal yields the single-beam spectrum, as shown in Figure 1.32.

An operating system of an instrument that is based on this principle, manufactured by TeraView Ltd. (Cambridge, UK), is shown in Figure 1.33 [82]. This

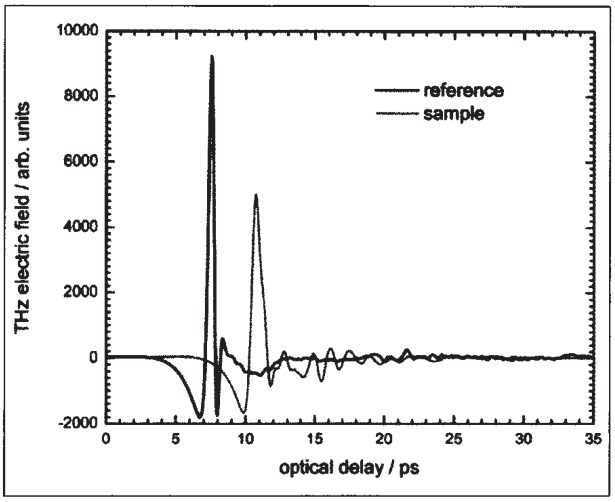

Figure 1.31 The terahertz electric field recorded as a function of time for the background (left centerburst) and when the beam passes through a 4 mm-thick silicon sample (right centerburst). Reproduced with permission from Ref. [79].

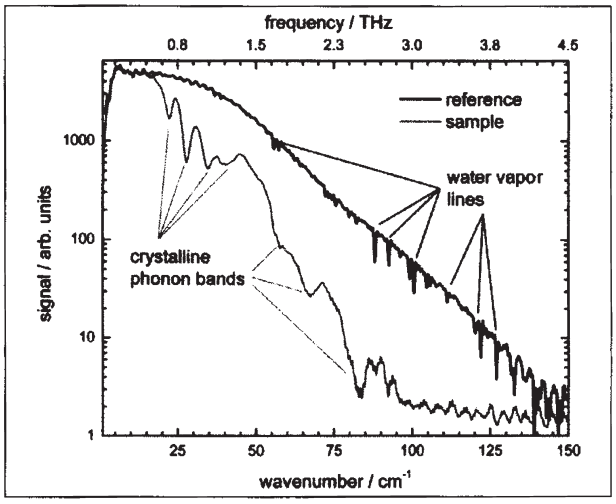

Figure 1.32 Fourier transforms of the two time domain waveforms shown in Figure 1.31. The signal is plotted on a logarithmic scale to show the dynamic range of the instrument. Pure rotation lines due to water vapor are seen on the background spectrum (above). The sample spectrum (below) is that of crystalline silicon. Reproduced with permission from Ref. [79].

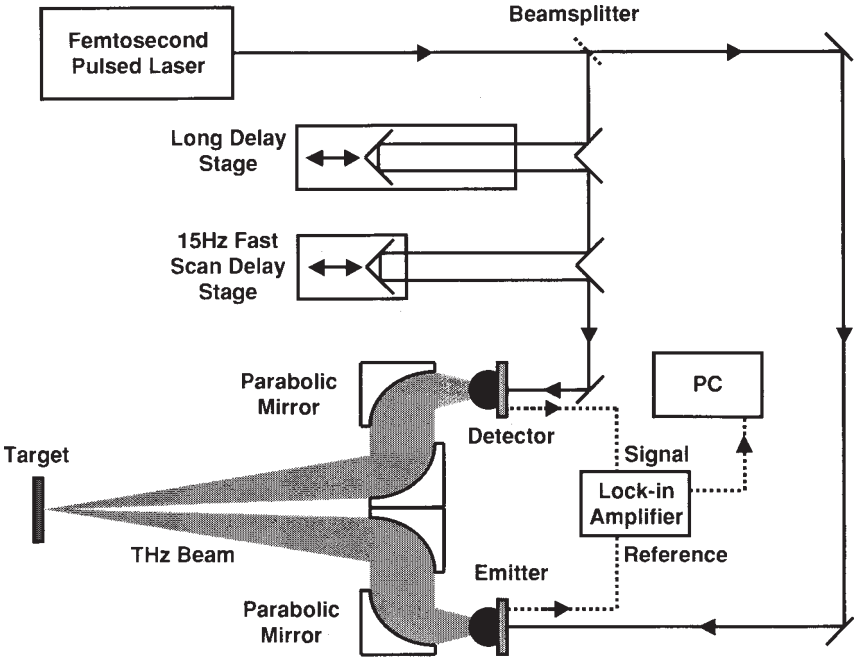

Figure 1.33 Schematic representation of a terahertz spectrometer. Reproduced with permission from Ref. [82].

spectrometer generates pulsed broadband terahertz radiation in the range of 0.05 to 4 THz (1.4 to 130 cm^{-1}). Measurements on this instrument can be recorded in two modes: (i) a rapid-scan mode, where the optical time delay is generated by mirrors that move rapidly and continuously and for which the maximum resolution is 1 cm^{-1}; and (ii) a step-scan mode where the time delay is generated by a cube-corner retroreflector the position of which is controlled by a stepper motor, where the maximum resolution is 0.1 cm^{-1}. The rapid-scanning delay line allows both the delay position and the output of the lock-in amplifier to be digitized and re-interpolated to obtain the THz field as a function of optical delay in real time.

Terahertz radiation has the major advantage that, because the wavelengths are so long, scattering is minimized. Thus, it is often possible to measure a THz transmission spectrum through a pharmaceutical tablet or cardboard packaging material. However, the absorption spectrum of water contains a very strong, broadband centered at 5.6 THz (17.9 cm^{-1}) which has been assigned to the resonant stretching of the hydrogen bond between the water molecules (although the present author believes that that mode should be observed at considerably higher frequency and the 5.6 THz band is more likely to be due to a bending or torsional mode of the hydrogen bond.) In any event, the high absorption of water in the THz region makes it possible to accomplish whole-body imaging [83], to observe the contrast between muscle and adipose tissue [84] and also between tumor and normal tissue [85].

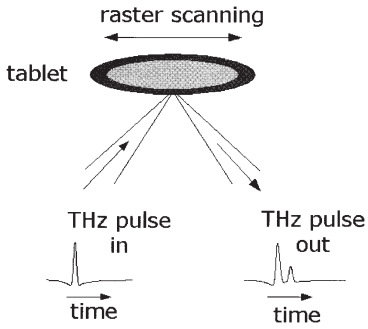

Figure 1.34 Schematic diagram of the experimental arrangement to examine the coating of a pharmaceutical tablet. Reproduced with permission from Ref. [86].

The spatial resolution in the *x* and y dimensions is determined by the diffraction limit (see Equation 1.3). Since λ is between ~70 and 700 μm, the resolution in these directions is far worse than for NIR or mid-IR microspectroscopy. On the other hand, significantly better resolution in the *z* direction may be obtained, since the THz pulse duration of <200 fs produces an axial resolution of 30 μm. The 3-D structure of the coating of pharmaceutical tablets has been studied by Fitzgerald *et al.* [86]. When the instrument is operated in the reflection mode, a reflected THz signal occurs whenever there is a change in boundary conditions; that is, the refractive index of two adjacent layers changes. This results in multiple pulses being returned to the detector, as shown schematically in Figure 1.34. Measurements of this type can be made in two ways: (i) one mode allows for a rapid single-point measurement of the coating thickness; alternatively (ii) multipoint measurements can be made by rastering the sample to allow false color maps of the uniformity of different layers to be produced.

An example of the time domain waveforms at several points on ibuprofen tablets from two different manufacturers is shown in Figure 1.35. The lower trace is for a tablet that has a single coating, whereas the upper trace is for a tablet with multiple coatings. By knowing the refractive index of each layer, its thickness can be calculated.

1.8 Summary

Powerful instruments for mapping and hyperspectral imaging in the NIR, mid-IR and far-IR regions, and by Raman spectroscopy, are now commercially available. Although instruments for imaging were initially expensive – frequently costing more than US$ 200 000 – the price tag continues to fall; for example, with the advent of rapid-scanning FPA imaging systems, the cost of mid-IR imaging

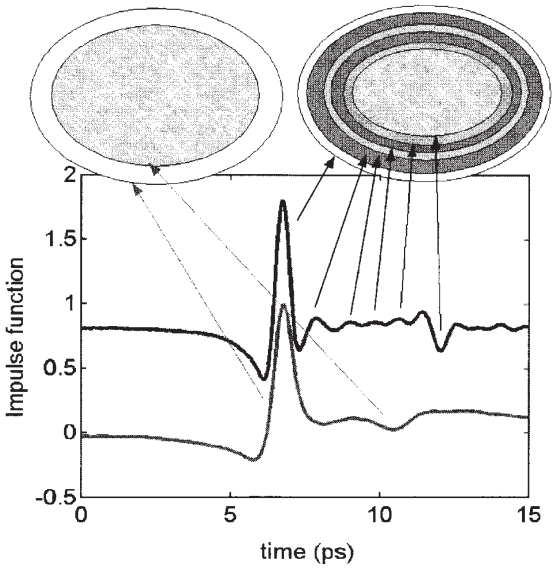

Figure 1.35 Example of depth profiling by terahertz spectroscopy. Pulses arise from interfaces between the coating layers, as illustrated by the schematic illustrations of the tablets. The lower trace is for the sample on the left, and the upper trace for the sample on the right. Reproduced with permission from Ref. [86].

spectrometers now starts from US$ 150 000. Instruments used for mapping measurements, where the spectra of single points on the sample are measured sequentially and the position of the sample is changed after each measurement, are less expensive than imaging spectrometers, but the measurements are much more time-consuming and the spectra, when measured with high spatial resolution, typically have a decreased SNR. The hybrid linear array mapping approach, although much faster than single-point mapping and with an increased SNR and spatial resolution, is still several-fold less efficient in terms of speed (time), SNR and spatial resolution than contemporary rapid-scanning, FPA-based chemical imaging systems. With NIR instruments, a similar comparison cannot be made, as most imaging measurements are made by changing the wavelength with an LCTF, and mapping NIR microspectrometers are rarely encountered. The situation is less definitive for Raman spectrometry, as mapping instruments are both sensitive and fast, especially with the development of electron-multiplying CCDs. In summary, it can certainly be said that hyperspectral imaging spectrometers are today revolutionizing the way in which vibrational spectroscopy is used, especially with respect to the analysis of pharmaceutical products and for medical diagnosis.

Acknowledgments

I would like to thank the Alexander von Humboldt Foundation for a senior research fellowship; most of this chapter was written while I was working in the Laboratory of Professor Reiner Salzer at the Technical University of Dresden. I owe a debt of gratitude to several people who read through the chapter and made many useful suggestions, including Fran Adar (Horiba Jobin-Yvon), Bruce Chase (du Pont), Neil Everall (at the time with ICI) and Bob Messerschmidt (Rare Light, Inc.) A particular word of thanks goes to Mustafa Kansiz (Varian) for reading the penultimate version of the chapter and suggesting several useful and important changes. Finally, I would like to thank Louise Ho (Cambridge University), who supplied me with a plethora of useful material on terahertz spectroscopy and imaging.

References

1 Lester, D.S., Kidder, L.H., Levin, I.W. and Lewis, E.N. (1998) *Cell. Mol. Biol.*, **44**, 29–38.
2 Lewis, E.N., Gorbach, A.M., Marcott, C. and Levin, I.W. (1996) *Appl. Spectrosc.*, **50**, 263–9.
3 Romeo, M.J., Dukor, R.K. and Diem, M. (2008) Introduction to spectral imaging, and applications to diagnosis of lymph nodes, in *Vibrational Spectroscopy for Medical Diagnosis* (eds M. Diem, P.R. Griffiths and J.M. Chalmers), John Wiley & Sons, Ltd, Chichester, UK, pp. 1–26.
4 Šašić, S. and Clark, D.A. (2006) *Appl. Spectrosc.*, **60**, 494–502.
5 Burch, C.R. (1947) *Phys. Soc. [London]*, **59**, 41–8.
6 Barer, R. and Cole, A.R.H. (1949) *Nature [London]*, **163**, 198–201.
7 Gore, R.C. (1949) *Science*, **110**, 710–11.
8 Blout, E.R., Bird, G.R. and Grey, D.S. (1950) *J. Opt. Soc. Am.*, **40**, 304–13.
9 Wood, D.L. (1950) *Rev. Sci. Instrum.*, **21**, 764–6.
10 Norris, K.P. (1954) *J. Sci. Instrum.*, **31**, 284–7.
11 Perkin-Elmer Instrument News (1951) Vol. 4, No. 4.
12 Rafferty, D.W. and Virnelson, R.C. (1997) *Spectroscopy*, **12** (5), 42–4.
13 Merklin, G.T. and Griffiths, P.R. (1997) *J. Chem. Phys. B*, **101**, 7408–13.
14 Griffiths, P.R. and de Haseth, J.A. (2007) *Fourier Transform Infrared Spectrometry*, 2nd edn, Wiley Interscience, Hoboken, NJ, pp. 277–81.
15 Griffiths, P.R. and de Haseth, J.A. (2007) *Fourier Transform Infrared Spectrometry*, 2nd edn, Wiley Interscience, Hoboken, NJ, pp. 161–8.
16 Williams, G.P. (2001) Synchrotron and free electron laser sources of infrared radiation, in *Handbook of Vibrational Spectroscopy*, Vol. 1 (eds J.M. Chalmers and P.R. Griffiths), John Wiley & Sons, Ltd, Chichester, UK, pp. 341–8.
17 Steiner, G., Sablinskas, V., Kitsche, M. and Salzer, R. (2006) *Anal. Chem.*, **78**, 2487–93.
18 Griffiths, P. R. and de Haseth, J.A. (2007) *Fourier Transform Infrared Spectrometry*, 2nd edn, Wiley Interscience, Hoboken, NJ, pp. 282–92.
19 Dumas, P. and Tobin, M.J. (2003) *Spectrosc. Eur.*, **15** (6), 17–23.
20 Levenson, E., Lerch, P. and Martin, M.C. (2006) *Infrared Phys. Technol.*, **49**, 45–52.
21 Miller, L.M. and Smith, R.J. (2005) *Vib. Spectrosc.*, **38**, 237–40.
22 Miller, L.M. and Dumas, P. (2006) *Biochim. Biophys. Acta*, **1758**, 846–57.
23 Dumas, P., Jamin, N., Teillaud, J.L., Miller, L.M. and Beccard, B.B. (2004) *Faraday Discuss.*, **126**, 289–302, discussion 303–11.

24 Everall, N., Lapham, J., Adar, F., Whitley, A., Lee, E. and Mamedov, S. (2007) *Appl. Spectrosc.*, **61**, 251–9.

25 Sommer, A.J. and Katon, J.E. (1991) *Appl. Spectrosc.*, **45**, 1633–40.

26 Smith, A.L. (1958) *Appl. Spectrosc.*, **12**, 153–9.

27 Romeo, M.J., Mohlenhoff, B. and Diem, M. (2006) *Vib. Spectrosc.*, **42**, 9–14.

28 Romeo, M.J., Boydston-White, S., Matthäus, C., Miljković, M., Bird, B., Chernenko, T., Lasch, P. and Diem, M. (2008) Infrared and Raman micro-spectroscopic studies of individual human cells, in *Vibrational Spectroscopy for Medical Diagnosis* (eds M. Diem. P.R. Griffiths and J.M. Chalmers), John Wiley & Sons, Ltd, Chichester, UK, pp. 27–70.

29 Mie, G. (1908) *Ann. Phys. (Leipzig)*, **25**, 377–452.

30 Walstra, P. (1964) *Phys. Br. J. Appl.*, **15**, 1545–52.

31 Hirschfeld, T. and Chase, B. (1986) *Appl. Spectrosc.*, **40**, 133–7.

32 Chase, D.B. and Rabolt, J.F. (1994) *Fourier Transform Raman Spectroscopy: From Concept to Experiment*, Academic Press, San Diego, CA.

33 McCreery, R.L. (2000) *Raman Spectroscopy for Chemical Analysis*, John Wiley & Sons, Inc., New York.

34 Sommer, A.J. and Katon, J.E. (1991) *Appl. Spectrosc.*, **45**, 527–34.

35 Delhaye, M. and Migeon, M. (1966) *Comptes Rendues Acad. Sci. Paris*, **262** (702-705), 1513–16.

36 Delhaye, M. and Dhamelincourt, P. (1975) *J. Raman Spectrosc.*, **3**, 33–43.

37 LaPlant, F. and Ben-Amotz, D. (1995) *Rev. Sci. Instrum.*, **66**, 3537–44.

38 Hollricher, O. and Ibach, W. (2007) Raman technology for today's spectroscopists. *Spectroscopy Supplement*, **June**, 38–43.

39 Cai, T.T., Zhang, D. and Ben-Amotz, D. (2001) *Appl. Spectrosc.*, **55**, 1124–30.

40 Savitzky, A. and Golay, M.C.E. (1964) *Anal. Chem.*, **36**, 1627–39.

41 Adar, F., Lee, E., Mamedov, S. and Whitley, A. (2006) *Spectroscopy Supplement: Raman*, **June**, 38–43.

42 Everall, N.J. (2007) Pittcon Conference and Expo, 2007, Chicago, IL, Paper 1820–5.

43 Macdonald, A.M. and Vaughan, A.S. (2007) *J. Raman Spectrosc.*, **38**, 584–92.

44 Pettinger, B. (2006) *Top. Appl. Phys.*, **103**, 217–40.

45 Zhang, W., Yeo, B.S., Schmid, T. and Zenobi, R. (2007) *J. Phys. Chem. C*, **111**, 1733–8.

46 Yeo, B.-S., Zhang, W., Vannier, C. and Zenobi, R. (2006) *Appl. Spectrosc.*, **60**, 1142–7.

47 Yeo, B.-S., Schmid, T., Zhang, W. and Zenobi, R. (2007) *Anal. Bioanal. Chem.*, **387**, 2655–62.

48 Hayazawa, N., Watanabe, H., Saito, Y. and Kawata, S. (2006) *J. Chem. Phys.*, **125**, 244706/1–244706/7.

49 Neugebauer, U., Roesch, P., Schmitt, M., Popp, J., Julien, C., Rasmussen, A., Budich, C. and Deckert, V. (2006) *Chem. Phys. Chem.*, **7**, 1428–30.

50 Roy, D., Wang, J. and Welland, M.E. (2006) *Faraday Discuss.*, **132**, 215–25.

51 Abrahamsson, C., Johansson, J., Andersson-Engels, S., Svanberg, S. and Folestad, S. (2005) *Anal. Chem.*, **77**, 1055–105.

52 Abrahamsson, C., Lowgren, A., Stromdahl, B., Svensson, T., Andersson-Engels, S., Johansson, J. and Folestad, S. (2005) *Appl. Spectrosc.*, **59**, 1381–7.

53 Chauchard, F., Roger, J.M., Bellon-Maurel, V., Abrahamsson, C., Andersson-Engels, S. and Svanberg, S. (2005) *Appl. Spectrosc.*, **59**, 1229–35.

54 Johansson, J., Folestad, S., Josefson, M., Sparen, A., Abrahamsson, C., Andersson-Engels, S. and Svanberg, S. (2002) *Appl. Spectrosc.*, **56**, 725–31.

55 Tsuchikawa, S. and Tsutsumi, S. (2002) *Appl. Spectrosc.*, **56**, 869–76.

56 Delphy, D.T., Cope, M., van der Zee, P., Arridge, S., Wray, S. and Wyatt, J. (1988) *Phys. Med. Biol.*, **33**, 1433–42.

57 Long, W. and Burns, D. (1997) *Anal. Chim. Acta*, **348**, 553–63.

58 Averett, L.A. and Griffiths, P.R. (2008) *Appl. Spectrosc.*, **62**, 377–82; 383–88.

59 Hudak, S.J., Haber, K., Sando, G., Kidder, L.H. and Lewis, E.N. (2007) *NIR News*, **18** (6), 68.

60 Treado, P. J. and Nelson, M.P. (2001) Raman imaging, in *Handbook of Vibrational Spectroscopy*, Vol. 2 (eds J.M. Chalmers and P.R. Griffiths), John Wiley

& Sons, Ltd, Chichester, UK, pp. 1429–59.
61 Christensen, K.A. and Morris, M.D. (1998) *Appl. Spectrosc.*, 1145–8.
62 Zhang, D., Hanna, J.D., Jiang, Y. and Ben-Amotz, D. (2001) *Appl. Spectrosc.*, **55**, 61–5.
63 Goldstein, S.R., Kidder, L.H., Herne, T.M., Levin, I.W. and Lewis, E.N. (1996) *J. Microsc.*, **184**, 35–45.
64 Suhre, D.R., Gottlieb, M., Taylor, L.H. and Melamed, N.T. (1992) *Opt. Eng.*, **31**, 2118–23.
65 Vo-Dinh, T., Stokes, D.L., Wabuyele, M.B., Martin, M.E., Soon, J.M., Jafannathan, R., Michaud, E., Lee, R.J. and Pan, X. (2004) *IEEE Eng. Med. Biol. Mag.*, Sept/Oct, 40–9.
66 Lewis, E.N., Treado, P.J., Reeder, R.C., Story, G.M., Dowrey, A.E., Marcott, C. and Levin, I.W. (1995) *Anal. Chem.*, **67**, 3377–81.
67 Snively, C.M., Katzenberger, S., Oskarsdottir, G. and Lauterbach, J. (1999) *Opt. Lett.*, **24**, 1841–3.
68 Snively, C.M. and Koenig, J.L. (1999) *Appl. Spectrosc.*, **53**, 170–7.
69 Bhargava, R. and Levin, I.W. (2005) Fourier transform mid-infrared spectroscopic imaging, Ch. 1 in *Spectrochemical Analysis Using Infrared Multichannel Detectors* (eds R. Bhargava and I.W. Levin), Blackwell Publishing Ltd, Oxford, UK, pp. 1–24.
70 Harrick, N.J. (1967) *Internal Reflection Spectroscopy*, John Wiley & Sons, Inc., New York.
71 Burka, E.M. and Curbelo, R. (2000) US Patent No. 6,141,1000.
72 Sommer, A.J., Tisinger, L.G., Marcott, C. and Story, G.M. (2001) *Appl. Spectrosc.*, **55**, 252–6.
73 Chan, L.A. and Kazarian, S.G. (2003) *Appl. Spectrosc.*, **53**, 381–9.
74 N.J. Everall (2007) ATR Imaging. Meeting of the Infrared and Raman Discussion Group, Sheffield, UK, April 2007.
75 Thomson, G.A. and Poulter, G. (2007) GB Patent No. 6,661,573.
76 Davis, J.R. (2003) US Patent No. 6,661,573.
77 Ricci, C., Bleay, S. and Kazarian, S.G. (2007) *Anal. Chem.*, **79**, 5771–6.
78 Griffiths, P.R. (2001) Far infrared spectroscopy, in *Handbook of Vibrational Spectroscopy*, Vol. 1 (eds J.M. Chalmers and P.R. Griffiths), John Wiley & Sons, Ltd, Chichester, UK, pp. 229–39.
79 Taday, P.F. and Newnham, D.A. (2004) *Spectrosc. Eur.*, **16** (5), 20–4.
80 Pickwell, E. and Wallace, V.P. (2006) *J. Phys. Appl. Phys.*, **39**, R301–10.
81 Auston, D.H., Cheung, K.P., Valdmanis, J.A. and Kleinman, D.A. (1984) *Phys. Rev. Lett.*, **53**, 1555–8.
82 Baker, C., Tribe, W.R., Cole, B.E. and Kemp, M.C. (2005) Developments in people screening using terahertz technology in optics and photonics for counterterrorism and crime fighting (eds T.P. Donaldson and C. Lewis), Proceedings, Optics and Photonics for Counterterrorism and Crime Fighting, SPIE, Bellingham, WA 2005, Vol. 5616, pp. 61–8.
83 Siegel, P.H. (2004) *IEEE Trans. Microw. Theory Tech.*, **52**, 1538–47.
84 Fitzgerald, A.J., Berry, E., Zinv'ev, N.N., Homer-Vanniasinkam, S., Miles, R.E. and Smith, M.A. (2003) *J. Biol. Phys.*, **129**, 123–8.
85 Pickwell, E., Fitzgerald, A.J., Cole, B.E., Pye, R.J., Ha, T., Pepper, M. and Wallace, V.P. (2005) *J. Biomed. Opt.*, **10**, 064021.
86 Fitzgerald, A.J., Cole, B.E. and Taday, P.F. (2005) *J. Pharm. Sci.*, **94**, 177–83.